Simulation of Medical Irradiation and X-Ray Detector Signals

Der Naturwissenschaftlichen Fakultät
der Friedrich-Alexander-Universität
Erlangen-Nürnberg

zur

Erlangung des Doktorgrades Dr. rer. nat.

vorgelegt von

Björn Kreisler
aus Frankfurt am Main

Als Dissertation genehmigt
von der Naturwissenschaftlichen Fakultät
der Friedrich-Alexander Universität Erlangen-Nürnberg

Tag der mündlichen Prüfung:	8. Februar 2010
Vorsitzender der Promotionskommission:	Prof. Dr. Eberhard Bänsch
Erstberichterstatterin:	Prof. Dr. Gisela Anton
Zweitberichterstatter:	Prof. Dr. Stanislav Pospisil

Contents

Introduction

The World Health Organisation (WHO) runs a program to classify the causes of mortality called the *International Statistical Classification of Diseases (ICD)*. This classification has its origins in the 1850s and has been part of the WHO since 1948 when the sixth version of the ICD was published. The latest version (*ICD-10, Version 2007*) outlines two major mortality reasons in the member states of the WHO: *Diseases of the circulatory system* and *Neoplasms*.
In modern societies, the early diagnosis of tumours is one aim of the routine medical checks. But even in the case of a diagnosis, the treatment of tumours requires deeper medical and physical knowledge. A case dependent combination of surgery, chemotherapy and irradation offers the best chance to cure the disease. In chemotherapy, drug medication is used to reduce the tumour size and growth, but the complete body has to cope with the drug. Irradiation medicates the tumour cells by depositing energy inside the tumour tissue, destroying the DNA (desoxyribonucleic acid - the long term carrier of genetic instructions) inside the cell nucleus and thereby forcing the cells into apoptosis. The irradiation is possible with different sorts of particles: electrons, photons, protons or heavy ions. The choice between the different irradiation options is guided by the need to protect the surrounding healthy tissue from dose deposition. As facilities for proton or heavy ion irradiation are rather large and expensive and not suitable for all cases, most irradiation is performed with photons and electrons.
Electron or photon beams are generated by accelerating electrons in a linear accelerator and then widening and flattening the beam by scattering foils. In the case of photon irradiation, a target is part of the beamline where photons are generated by Bremsstrahlung. The beam shaping is performed by collimation units which confine the beam laterally. For electron irradiation, the collimation is additionally performed by applicators to limit the electron beam dimensions close to the patient to reduce the divergency of the beam. The irradiation of the tumour tissue is planned based on computed tomography data using simplified Monte-Carlo tools. The beam input data for these planning systems are gained by measurements of the beam characteristics. The beam shape and homogeneity are commonly measured by films and dose chambers, which are both indirect measures as the deposited energy inside a given small volume is determined. Thereby, the information of the spectral distribution of the beam is lost, although this knowledge would be interesting as the penetration depth varies strongly with the initial energy. The measurement of the spatial and spectral distribution of the beam is technically difficult because the flux inside the beam is very large.
The complete beam characteristics can therefore only be acquired by a detailed simulation or by a new detector which can handle the flux in the beam. State of the art X-ray detectors are based on a semiconductor sensor layer which converts the incoming flux of photons (or high energy electrons) into electron hole pairs, which are then translated into an electronic signal. The separation of single interactions of the incoming particles can be

achieved. The signal shape and deposited energy per electron can be used to determine the spectral information of the incoming beam. Furthermore, if the sensor is pixelated, the detection can even be carried out with a spatial resolution. Nonetheless, the exact knowledge of the signals which are generated by the incoming beam is essential for the design of a detector.
The following work is separated in two main parts. In the first part, the design of a detector for X-rays is the central point. The signal generation after the interaction of an X-ray photon in the sensor will be explained. The influence of the geometrical dimensions and applied voltages is investigated and can be used to provide a guide for the design of the readout electronics. In the second part, the main focus is on the medical irradiation. Beginning with the basics of dosimetry and tumour treatment, the simulation of a medical irradiation system will be presented followed by the analysis of some parameters for the understanding of the systematics of the medical irradiation.
Together, both parts can show a way to improve the quality of medical irradiation. The enhanced knowledge on the beam parameters can be compared to accurate measurements with possible new detectors. And the advanced development of medical irradiation systems will improve by making use of simulations which offers an elegant way for optimisation.

Part I

Semiconductor Detector Signals

1 Basics of the Signal Calculation for Semiconductor X-Ray Detectors

Digital state of the art X-ray detection is realised either by scintillation or semiconductor systems. In comparison to the analog film (or digital storage phosphor) systems, the digital detection systems show a linear response over a wide energy and intensity range and can be used in multi imaging devices like computed tomography.
Scintillation and semiconductor systems have a fundamental difference: the X-rays inside a scintillator system are detected indirectly by converting the X-rays into visible light and then taking an image of this visible light with a charge-coupled device camera. The following work will focus on the direct detection with a semicondutor sensor layer where the X-rays are immediately converted into charges which are then transferred to the readout electronics.
The charge drift by a static electric bias field can be described by the continuity equation. The signal which enters the electronics is induced during the charge motion, and this charge induction process can be calculated using the so called pseudo electric weighting field. The indicated electric fields, the motion process and the charge induction calculation will be presented in the following chapter. The chapter will start with a short introduction into semiconductor X-ray detector design and operating mode.

1.1 X-Ray Semiconductor Detectors

Digital X-ray detection can be divided into two major steps: energy transfer from the incoming X-ray photons to a sensor volume and collection of the generated charge signal by a dedicated electronics. These two steps can be very clearly observed when looking at the hybrid X-ray detector Medipix [1], which is drawn in the left of figure 1.1. A semiconductor sensor layer is bump bonded to the Medipix ASIC pixel by pixel. Therefore energy transfer takes place in the sensor layer, but signal processing is performed in the electronics below.
The dimensions of the detector are rather small: each square pixel has an edge length of $55\,\mu$m, and there are 256×256 pixels per sensor, which leads to a sensitive area of $1.98\,\mathrm{cm}^2$. The bump bonding can be altered in a way that not every electronic pixel is connected to the sensor layer. This leads to fewer but larger pixels as the area of the ASIC is limited. An option to enlarge the sensitive area is to tile a larger area with more readout ASICs. As the ASIC is three side buttable, a large sensitive area with a width of 512 pixels can be constructed.
In the right part of figure 1.1, a cross-section though a sensor layer is drawn. An incoming X-ray photon interacts with the sensor material and free charge carriers are generated. As a bias voltage is applied across the sensor layer, i.e. the z-direction, the charge carriers will be separated and drift with respect to their charge sign towards the electrodes. One

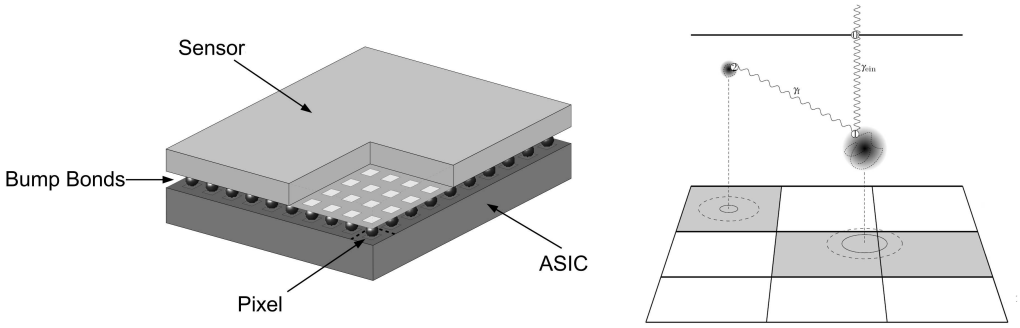

Figure 1.1 Left: simplified drawing of the hybrid layout of the Medipix detector [2]. The sensor layer is bump bonded to the pixelated ASIC. Right: cross-section through the sensor layer of a semiconductor detector [3]. The incoming X-ray interacts via a photo effect and generats a charge cloud. A thereby occuring fluoresence photon generates another charge cloud in an adjacent pixel. Both charge clouds are moved to the electrodes by an applied electric bias field. The projected charge cloud is drawn with a solid line, but diffusion leads to a larger area (dotted line).

side of the sensor layer has a pixelated electrode to allow a measurement of the lateral position, i.e. x- and y-direction. The charge signal in each electrode will be transferred to the electronics by the bump bond contact. Each pixel electrode processes the incoming signal and compares the signal to an adjustable threshold. If the threshold is met, the electronics counts the event.
Due to the pixelated structure of the electrodes, the charge type (electrons or holes) which is collected at the pixelated electrodes takes the main part in the signal generation. This small pixel effect can be explained by the weighting potential and will be addressed in chapter 1.3.
An obvious problem with this kind of pixelated structure is the distribution of the generated charge to more than one electrode. The distribution can to some extend be restored by the electronics of the oncoming Medipix3 [4], where neighbouring pixel cells are interconnected and sum up their signals. As the Medipix is a charge sensitive detector, the energy selective single photon counting mode count rate is limited and an improvement may be achieved by measuring the currents instead of the collected charges. This needs an exact knowledge of the signal shape and timing.

1.2 Electric Fields in Matter

The electric potential Φ inside a medium is described by the Poisson equation [5],

$$\Delta\Phi = \vec{\nabla}\vec{E} = -\frac{\rho}{\epsilon\epsilon_0} \tag{1.1}$$

where ρ is the space charge density, ϵ_0 is the vacuum permittivity and ϵ is the relative permittivity of the material. The electric field $\vec{E}$ is the gradient of the potential Φ.

1.2.1 Bias Field

The electric potential of the voltage U_{bias} which is applied across a sensor layer of thickness d leads to a homogeneous electric field ($\vec{E} = \frac{U_{bias}}{d}$) inside the material. As the potential is set to a fixed value on one side and to ground on the other (pixelated) side, the field is directed from one side to the opposite like in a plate capacitor. A plate capacitor can be filled with an insulating material (with a relative permittivity ϵ) which alters the local electric field strength, but is leaving the main character of the field unchanged: the electric field has a constant value $E = \frac{U_{bias}}{\epsilon d}$ throughout the volume.
Inside a semiconductor, the electric field strength may vary due to the doping (i.e. locally fixed space charges) of the material which allows free charges to move through the material. A homogeneous space charge density ρ can be calculated by

$$\rho = \frac{2\epsilon\epsilon_0 U_d}{d^2} \tag{1.2}$$

which depends on the depletion voltage U_d, the material parameter ϵ and the thickness d. The electric field distribution in the doped material is inclined compared to the undoped case. The difference is depending on the doping level (i.e. the depletion voltage) of the material [6]. In figure 1.2, the inclination of the electric field is shown for the undoped case as well as for an n- and p-doped material. The measurement of the electric field can be performed using the Pockels effect where the polarisation direction of the incoming light is rotated due to the electric field strength [7].
In case the electrodes do not cover the whole pixelated area, an additional effect occurs: the electric field is constricted close to the pixelated electrodes. This modification not only changes the shape of the field, but also the strength close to the pixelated electrodes is increased. As the electric potential is unchanged, the electric field strength in the bulk of the material is decreased to compensate for the increase close to the pixelated electrodes. These variations to the electric field shape and strength have to be taken into account when solving the Poisson equation.

1.2.2 Weighting Field

Charges in the proximity of electrodes induce mirror charges on the electrodes. Inside a plate capacitor electrode configuration, the mirror charges are induced on both plates in a similar way. In the case of a pixelated electrode setup, the mirror charges are spread over the electrodes and each pixel electrode will encounter only a fraction of the mirror charge. The motion of the charges in the volume leads to a motion of the mirror charges in the electrodes.
The pseudo electric weighting potential is part of the Shockley-Ramo Theorem [8, 9] to calculate the instantaneously induced current on a given electrode i when a charge q is moving outside the electrode. The resulting induced current can be in- and out-flowing, depending on the motion direction of the charge q. The integral over the induced current results in the induced charge. The amount of induced charge depends on the weighting potential difference between the start and end point of the motion of the charge q. The induced charge may be only temporarily, when the trajectory of the charge q s returning to the same weighting potential value at the end of the motion. The motion of the charge

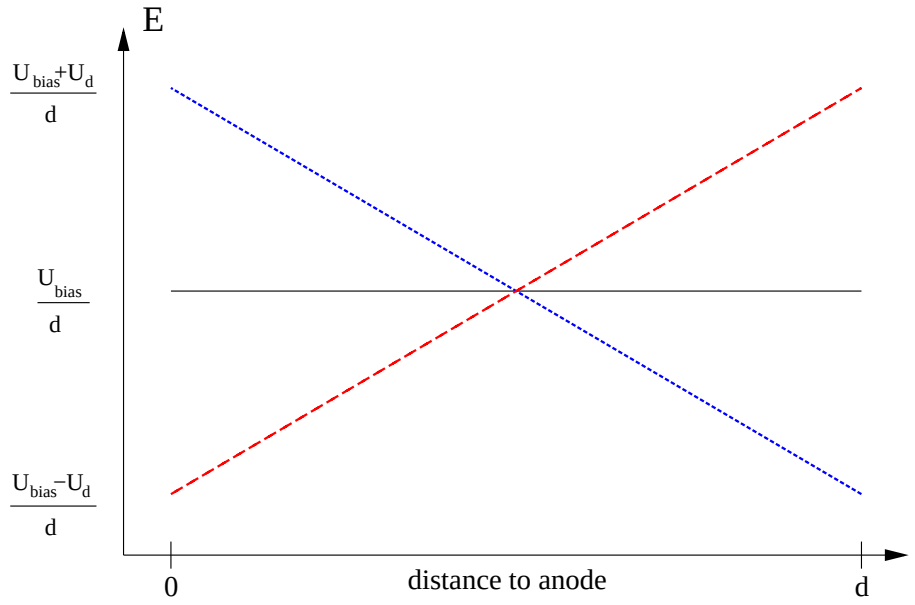

Figure 1.2 Electric field strength E inside a semiconductor in a plate capacitor-like electrode configuration as a function of the distance to one plate. The electric field is calculated by the bias voltage U_{bias} divided by the thickness of the semiconductor d. If a locally fixed space charge is present in the semiconductor, the depletion voltage U_d changes the local electric field strength. In the undoped case (solid line), the field strength is constant, in the n-doped (dashed line) and p-doped (dotted line) case, the electric field strength is a linear function of the distance towards the electrode.

q depends on the actual electric field at the position of the charge, which means the motion is not influenced by the weighting potential.
The weighting potential can be obtained by solving the Poisson equation for a very simple case: all electrodes are set to ground except the one of interest (electrode i) which is set to unit potential. The volume is treated like vacuum, meaning no space charge and no relative permittivity. The potiential includes values between zero and one. The weighting field $\vec{W}_i$ is the gradient of the weighting potential calculated this way. The weighting potential takes only geometrical aspects into account as no material properties are implemented in its calculation.

1.3 Charge Motion and Induced Currents

The electric bias field in the semiconductor sensor layer of an X-ray detector results in a drift of free charges. A charge cloud generated by an X-ray interaction will therefore drift with respect to the electric field. This drift motion is superimposed by a gradient driven diffusion and an inner electric repulsion.
The charge motion neglecting replusion can be described by a continuity equation of the charge concentration c

$$\frac{\partial c}{\partial t} - \vec{\nabla} \cdot (D\vec{\nabla}c) - \vec{\nabla} \cdot (c\,\vec{v}) = c_0 \tag{1.3}$$

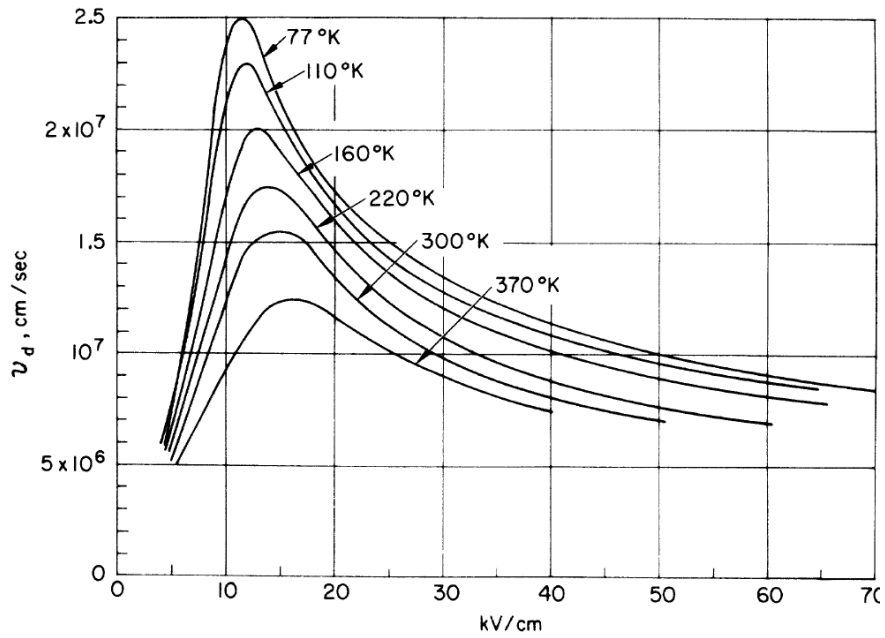

Figure 1.3 The electron drift velocity v inside CdTe is a function of the electric field strength [10]. The slope of the function is the mobility μ, which is used to couple the motion with the electric field.

where the drift velocity $\vec{v}$ is directly coupled to the electric field by the Einstein equation $\vec{v} = \mu\vec{E}$. The mobility μ is a material parameter and depends on the electric field strength. In figure 1.3, the variation of the electron velocity in CdTe is plotted as a function of the electric field. For other materials like silicon, the graph reaches a finite value for high electric fields, i.e. a saturation velocity [11]. The isotropic diffusion is parametrised by the coefficient D. The initial charge distribution c_0 is placed at the interaction point of the incoming X-ray photon [12]. The transient flux $\vec{F}$ of this initial charge cloud is then available,

$$\vec{F}(t) = c(t)\,\vec{v} + D\,\vec{\nabla}c(t). \tag{1.4}$$

The motion of the charge cloud (see figure 1.4) leads to a motion of the mirror charges in the electrodes. The current in the electrodes, i.e. the motion of the mirror charges, is induced during the motion of the charge cloud [13]. This effect can be described by the formalism proposed by Ramo [8]. The induction process makes use of the weighting field, as the geometrical setup of the sensor is coded in this pseudo electric field. The induced electric current $I(t)$ on the i$^{\text{th}}$ electrode can be obtained by integrating the scalar product of the charge flux $\vec{F}(t)$ and the weighting field $\vec{W}_{\text{i}}$ of the i$^{\text{th}}$ electrode over the complete sensor volume V_{s},

$$I(t) = \int_{V_{\text{s}}} \vec{F}(t) \cdot \vec{W}_{\text{i}}\, dV. \tag{1.5}$$

The collected charge on the electrode can be obtained by integrating the induced current over the collection time. This calculation results in a current and charge signal on the electrode of interest for a single interaction point of the X-ray photon. Signals from

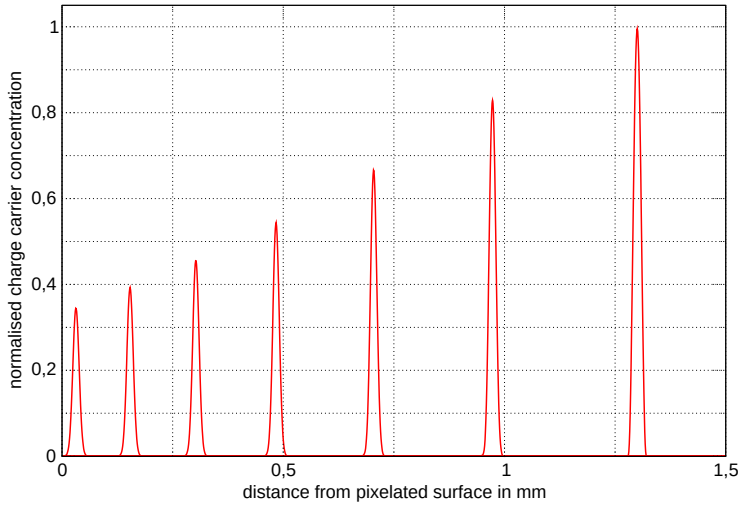

Figure 1.4 Stroboscopic view on a moving charge cloud with equal time stepping. The charge cloud starts on the right side and is moving to the left while the speed is decreasing due to a decrease of the electric field strength.

adjacent electrodes can be obtained by integrating the charge flux multiplied by the respective weighting field of the adjacent electrode [14].
The motion of the charge cloud has to be calculated for each possible starting point in the sensor and the integration for each electrode has to be performed subsequently. This leads to a considerable computing time for a reasonable density of starting points.

1.4 Adjoint Solution

To avoid this immense computing time, the adjoint solution was proposed by Prettyman [15]. An adjoint continuity equation can be constructed as the charge carrier continuity equation in the forward simulation involves linear operators [16, 17]. The continuity equation for the adjoint electron concentration c^+ is given by

$$\frac{\partial c^+}{\partial t} - \vec{\nabla} \cdot (D\vec{\nabla}c^+) + \mu\vec{E} \cdot \vec{\nabla}c^+ = c_0^+ \tag{1.6}$$

where D is the diffusion coefficient. When the initial adjoint electron concentration is set to $c_0^+ = \mu\vec{E} \cdot \vec{W}$, the solution leads to a spatial and temporal response function $c^+(\vec{r}, t)$ of the sensor. In figure 1.5, a stroboscopic view of the motion of the adjoint electron concentration is plotted. The current and charge signals for any starting point of the charge cloud can then be calculated from the response function.
In the case of undoped material, i.e. $\vec{\nabla} \cdot \vec{E} = 0$, the motion term of the adjoint continuity equation can be transformed

$$\mu\vec{E} \cdot \vec{\nabla}c^+ = \vec{\nabla} \cdot (\mu c^+ \vec{E}) = \vec{\nabla} \cdot (c^+ \vec{v}) \tag{1.7}$$

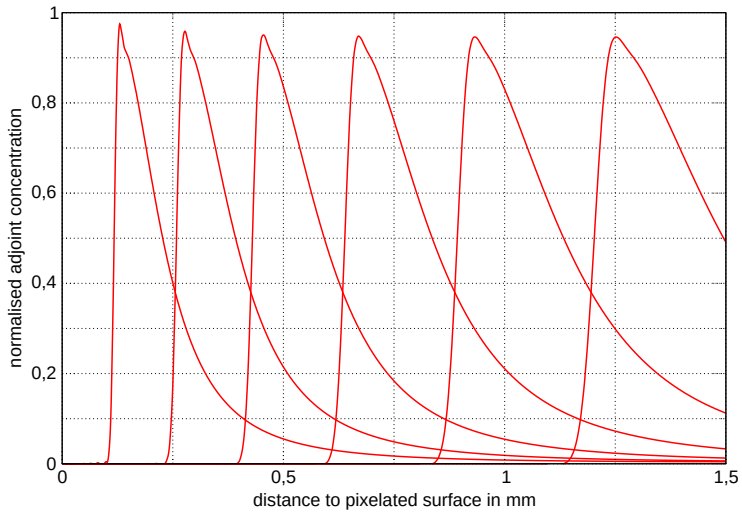

Figure 1.5 Stroboscopic view on the motion of the adjoint electron concentration with equal time stepping. The adjoint electron concentration starts on the left side and is moving to the right while the speed is increasing due to the electric field strength is increasing. The motion is in the opposite direction as the real charge motion.

which results in the possibility to apply the standard continuity equation for the case of the adjoint charge concentration c^+:

$$\frac{\partial c^+}{\partial t} - \vec{\nabla} \cdot (D\vec{\nabla}c^+) + \vec{\nabla} \cdot (c^+\vec{v}) = c_0^+ \tag{1.8}$$

where the sign of the drift term has changed and the initial adjoint charge concentration is set to $c_0^+ = \mu\vec{E} \cdot \vec{W}$. The solution $c^+(\vec{r}, t)$ is the time-dependent map (charge induction map (CIM)) of the adjoint charge concentration.
Here, the extraction of the induced signals is a lot more flexible than for the forward calculation (charge motion and electric induction). The backward calculation (adjoint solution) results in a response function (CIM) and a standard integration of the CIM over the volume of the initial charge cloud V_i results in the current

$$I(t) = \int_{V_\mathrm{i}} c^+(t)\, dV. \tag{1.9}$$

The integration of the current over time can be performed subsequently to acquire the collected charge. The time-dependent calculation has to be done just once for each geometrical setup, and the selection of the starting points is a postprocessing procedure. Even the signals for the adjacent electrodes can be calculated from the CIM by taking advantage of given symmetries.
This mapping leads to the opportunity to generate lookup tables which can be used together with Monte-Carlo data to simulate the complete detector response from the incoming X-ray photons to the signals arriving at the electronics [18]. The lookup table based simulation can cope with complete imaging devices like computed tomography to simulate imaging properties with a tuneable degree of precision.

1.5 Generalised Adjoint Solution

The main disadvantage of the adjoint solution is the restriction to undoped or only poorly doped materials. State of the art semiconductor sensor materials like CdTe or CdZnTe are intrinsically doped to a level, which cannot be treated sufficiently with the previously presented method [15].
The sensor layer of the hybrid X-ray detector Medipix which is investigated in the laboratory at the ECAP (Erlangen Centre for Astroparticle Physics) for spectral imaging purposes is made of CdTe. The inhomogeneity of the electric field due to doping is not negligible in this material. Therefore it was necessary to find a way to extend the simulation for this case.
As the adjoint continuity equation (see equation (1.6)) is not affected by the inhomogeneity of the electric field, the critical point is the transformation of the motion term [19]. The correct propagation of the $\vec{\nabla}$-operator in the motion term of the adjoint continuity equation leads to

$$\mu\vec{E}\cdot\vec{\nabla}c^{+} = \vec{\nabla}\cdot(\mu c^{+}\vec{E}) - \mu c^{+}\vec{\nabla}\cdot\vec{E} = \vec{\nabla}\cdot(c^{+}\vec{v}) - \mu c^{+}\vec{\nabla}\cdot\vec{E} \tag{1.10}$$

which is true even if the electric field has a spatial variation due to doping. The additional term vanishes in the case of no inhomogeneities. The restriction of the adjoint solution to undoped material can thus be overcome by adding a term to the continuity equation [20],

$$\frac{\delta c^{+}}{\delta t} - \vec{\nabla}\cdot(D\vec{\nabla}c^{+}) + \vec{\nabla}\cdot(c^{+}\vec{v}) - \mu c^{+}\vec{\nabla}\vec{E} = c_0^{+}. \tag{1.11}$$

The equation is very similar to equation (1.8), but the additional term adjusts the integral over the complete response function. The adjustment leads to a correction of the induced current signal height, and therefore corrects the amount of collected charge. The compensation is not limited to homogeneous doping, it can cope with a locally variing doping profile as well.
The calculation of an induced signal $I(t)$ is performed like for the standard adjoint solution by integrating the CIM over the initial charge cloud volume V_i as in equation (1.9). The induced signals can again be integrated over time to get the collected charge.
The generalised adjoint solution allows the generation of a CIM for doped semiconductor sensor materials. This is an important improvement for applying the method to detectors like CdTe, which are needed for medical applications.

2 Signal Simulation

The transient motion of the charge concentration and of the adjoint charge concentration are described by partial differential equations which can be solved numerically. The commercial finite element simulation tool COMSOL Multiphysics [21] was used for this purpose.

2.1 Finite Element Simulation

The software offers the possibility to design the geometrical setup in two or three dimensions, taking possible symmetries into account. In the case of square pixels, a complete three-dimensional setup has to be used. In order to keep control over the computing time and memory usage, the volume of the simulation can be reduced without losing information when a sufficient symmetry is present as shown in figure 2.1, but also the design of the finite elements inside the volume can be optimised. In regions of strong gradients, i.e. strong electric fields or concentration gradients, the sampling needs to be very dense, whereas in regions of smooth gradients, the element size can be larger. The meshing

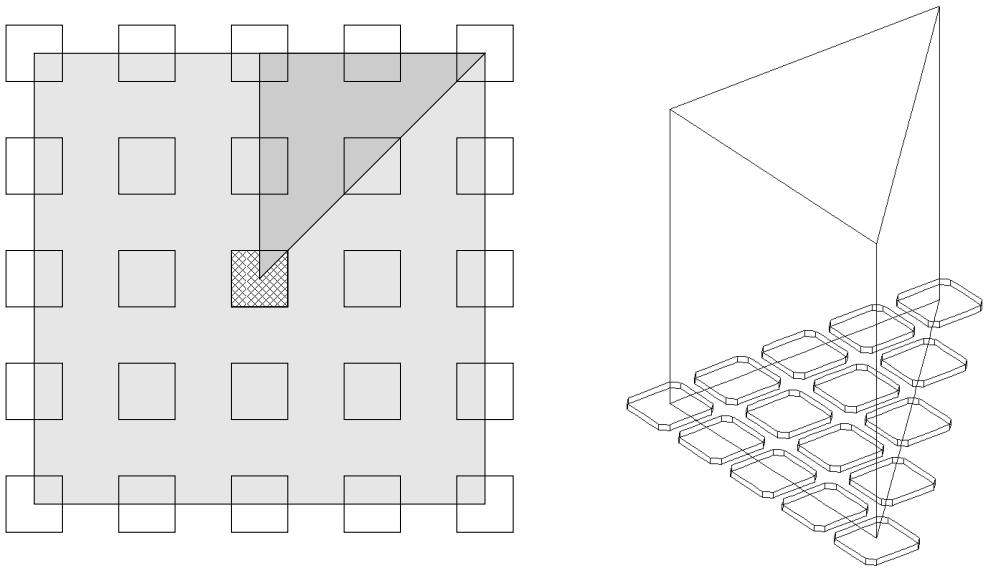

Figure 2.1 Left: top-view on a part of the pixelated surface of the sensor. A possible reduction of the simulation volume is indicated. The light grey area includes all possible X-ray interaction points which will induce significant signals on the central electrode (cross-hatched). This area can be covered by simulating the dark grey area and then taking advantage of the symmetry. Right: full 3D geometry used for the transient simulation.

algorithm can be tuned by defining growth rates, maximum element sizes and resolution parameters for different parts of the geometry separately. The mesh for each simulation has to be adjusted to the simulation parameters.

2.2 Static Electric Fields

To be able to use the electric field for the drift motion, the calculation of the electric bias field inside the sensor material has to be performed before the transient charge motion. In the setup used, the sensor surfaces were all set to the preconfigured boundary condition *symmetry*, which means $div\vec{E} = 0$. The pixelated electrodes are connected to *ground* (i.e. $U = 0\,\mathrm{V}$), whereas the opposite electrode is set to the finite bias potential, which selects the sort of charges to be collected at the pixelated electrodes. The simple change of the sort of collected charge cannot be performed in a real setup, as the doping of the material plays a role as well. The doped sensor layer is operated in reverse bias, so no current flows without the interaction of incoming X-rays.
The doping of the material is introduced by adding the space charge density as a volume parameter. This parameter can be implemented as a constant, but also as a closed form function. This allows the use of doping profiles, which can be obtained from measurements.
The calculation of the weighting field is also done inside the finite element simulation. The sensor surfaces are again set to *symmetry*. The electrode for which the simulation is performed is set to unit potential, whereas all other electrodes are set to *ground* according to Ramo's theorem. The volume has neither space charge nor relative permittivity, but is treated like vacuum.
Special attention has to be paid to the symmetries of the electric fields: the shape of the bias field is repeating each pixel pitch, but the weighting field is ranging to infinity. The simulation volume has to cover enough pixel cells to allow the weighting field to approach the final shape. Electrodes which are very far away from the central electrode do not affect the weighting potential significantly, but neglecting the influence has to be performed with caution.

2.3 Charge Motion and Electric Induction

The charge motion can be modelled as a concentration motion within the COMSOL software using the *Convection and Diffusion Model* [14]. The electric repulsion is neglected in this approach. The initial charge cloud, i.e. concentration distribution, is modelled by a smooth cap to suppress unphysical diffusion gradients.

$$c_0 = \left(1 + cos\left(\frac{\pi r}{r_0}\right)\right)(r < r_0) \tag{2.1}$$

With this function, the concentration has its maximum in the centre (x_0,y_0,z_0) and with increasing radial distance $r = \sqrt{(x-x_0)^2 + (y-y_0)^2 + (z-z_0)^2}$ the concentration is decreasing and slowly reaching zero at the boundaries of the sphere with radius r_0.
All sensor surfaces are set to *zero*, i.e. $c = 0$, so any concentration touching the boundaries

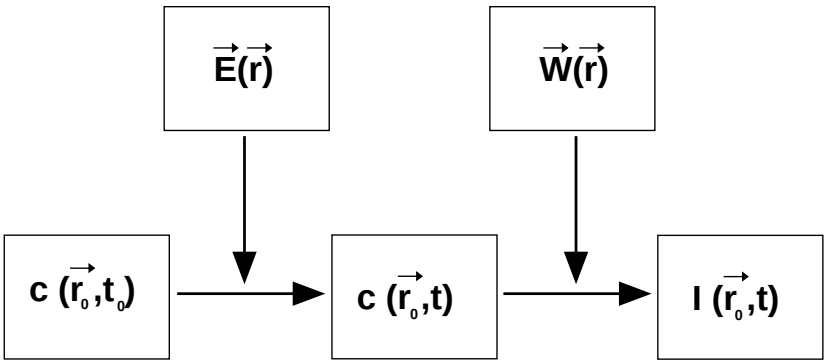

Figure 2.2 Flow chart of the simulation of the charge motion and the followup signal generation.

vanishes. The drift speed of the concentration $\vec{v}$ is coupled to the previously calculated electric bias field $\vec{E}$ by the mobility μ, which can be implemented as a constant or as a closed form function. The advantage of a closed form function is the option to include the dependency of the mobility on the electric field strength: $\mu = \mu(|\vec{E}|)$ (see figure 1.3). As the electric field strength inside the geometry used is between 5 and 10 $\frac{\mathrm{keV}}{\mathrm{cm}}$, the mobility can be assumed to be constant. The diffusion is added isotropically, but can also be implemented as a tensor to account for material properties. The transient simulation of the motion results in the flux of the concentration $\vec{F}(t)$.
This flux can now be converted into an electric signal by applying the weighting field $\vec{W}_{\mathrm{i}}$ of the electrode of interest. The integral over the sensor volume of the scalar product of the flux and the weighting field leads to the induced current for the specific starting point (x_0,y_0,z_0). For each starting point needed, the finite element simulation has to be performed separately. A flow chart of the process is shown in figure 2.2.
The simulation of a mixture of drift and diffusion motion has to cope with the dimensionless Peclet number [22] which is a ratio between the drift and diffusion motion. For the finite element simulation, this ratio is weighted with the element size to calculate the *cell peclet value* $= \frac{a|\vec{v}|}{D}$ where a is the element size, $|\vec{v}|$ is the drift speed and D is the diffusion coefficient. This value is ideally between zero and one. As values below 500 show good results, the criteria can be adopted to the available computing power. The cell peclet value has to be kept under observation and serves as an indicator for the stability of the simulation.

2.4 Adjoint Solution and Charge Induction Map

The solution of the adjoint equation system can also be done by the *Convection and Diffusion Model* in COMSOL [23]. In this case, the sensor volume is not just initialised with a single smooth cap somewhere in the middle, but the whole volume is covered with the inital condition $c_0 = \mu\vec{E} \cdot \vec{W}$. This results in different boundary conditions: all surfaces are set to *symmetry* ($div\, c = 0$), except the outflowing opposite electrode which is set to *convective flux* (no diffusion accross the boundary).
The motion of the adjoint concentration is coupled to the electric bias field, but in the

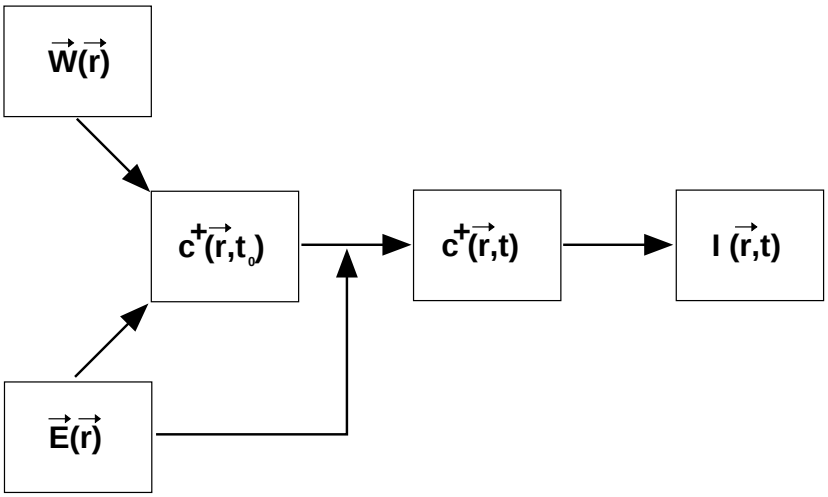

Figure 2.3 Flow chart of the simulation of the adjoint charge motion and the followup signal generation.

opposite direction compared to the real charge motion. The diffusion is implemented the same way as in the forward model.
The result of the transient simulation is a temporally resolved map of the adjoint concentration motion - the *charge induction map (CIM)*. The generation of the signals can be done during postprocessing, where several starting points can be read out. The volume of the integration area can be used to normalise the signal to the unit signal generated by a single electric charge. The normalised integration of the *CIM* over time leads to the *charge induction efficency map (CIE)*. A flow chart of the process is shown in figure 2.3.
The electric repulsion can be modelled during postprocessing by modifying the integration volume V_i. The radius of V_i is increased, but the integral over the volume has to be held at constant level. A possible model for the repulsion is based on a spherical time-dependent radius increase [24]. As the initial charge in the finite element simulation cannot be set to a point, but already has a finite volume at the starting time, the time in the repulsion model has shifted to $t + t_0$. The effect results in only a tiny change of the signal in the evaluated setups, but may gain importance in alternative geometries.
The modification of V_i can also be used to model the short time trapping of charges in the sensor material: the increase of the radius can be applied only in the motion direction of the charges which is equal to an effective change of the mobility. Another way to model the short term trapping is to superimpose many signals of single charges all arriving at different times. The time distribution of the arriving charges includes the trapping probability of the charges. This models the late arrival of trapped charges at the electrode and results in a tail in the signal. This tail heavily depends on the trapping probability.
The overall recombination and long term trapping only reduces the amount of charges which take part in the induction process for the main signal. As the drift times in the sensor are very short in comparison to the recombination time, the reduction of the charge amount can be implemented by an exponential decrease of the charge amount. However, the effect is very small in the evaluated setups and less than 2% of the charges get lost during the drift process.

3 Results

The results presented in the following section were all obtained by the finite element simulation tool COMSOL as described in the last section. The analysis and postprocessing of the signals was performed with Matlab [25].
In the standard setup used for simulation the sensor layer is made of CdTe, which has an intrinsic n-type doping of $2.6 \times 10^{11} \frac{1}{cm^3} \mathrel{\widehat{=}} 0.042 \frac{As}{m^3}$ (depletion voltage $U_d = 600\,V$). As the thickness is 1500 μm, the applied bias voltage is set to 900 V to achieve overdepletion with respect to the doping of the material. The pixelated surface is divided in square areas. The pixel pitch is 220 μm and the square electrodes have an edge length of 100 μm and are positioned in the centre of the pixel. The corners of the electrodes are truncated to lower the effects of superelevation in the electric field. The collected charges are the electrons, as the velocity of the holes is a factor of ten smaller than for the electrons and therefore the hole signals have no application for fast detection. These values are close to a prototype chip based on the Medipix which is used in the laboratory at the ECAP (Erlangen Centre for Astroparticle Physics) for imaging purposes and have therefore been used in the simulation to improve the understanding of the system behaviour.

3.1 Electric Fields

The electric fields are calculated for each setup of the sensor material. An example setup is plotted in figure 3.1. The streamline plot is a cut through the centre of the pixel electrodes and is oriented perpendicular to the pixel edges. The constriction of the field lines close to the pixelated surface results in an increased electrical field strength close to the electrodes.
Inside a plate capacitor, the electric potential has a linear slope. Hence, the electric field is a constant throughout the sensor. But inside a doped material, the electric field strength also varies as a function of the distance from the electrodes [26]. In the case of two homogeneously contacted electrodes on both sides of the sensor material, the electric field has a linear slope due to the doping. When the electrode on one side of the material is pixelated as needed for an imaging system, the electric field strength is modified: over the main part of the sensor, the field strength is decreased, but close to the pixelated electrode the field strength rises to higher values. In figure 3.2, the field strength is plotted as a function of the distance from the centre of a pixelated electrode. If the electrodes only cover a small fraction of the pixel area, the effect of the constriction is even more prominent.
The weighting potential is also calculated with the electrostatic module of the finite element simulation. Each configuration of pixel size, electrode size and sensor thickness leads to different weighting potentials. The case of a plate capacitor can again be used as a comparison to understand the meaning of the weighting field. Inside a plate capacitor, the weighting potential has a constant slope when plotting the potential as a function of the distance from one surface. If one side of the sensor layer is pixelated, the weighting

Figure 3.1 Electric field lines (red, vertical) and electric potential (blue, horizontal) for a doped CdTe sensor with the standard setup parameters. The pixelated electrodes are drawn as small boxes at the bottom of the sensor layer. The increase of the electric field strength, i.e. the density of the field lines, close to the pixelated electrodes can be clearly seen. The slope in the electric potential can be observed by the varying distances of the equally separated potential field lines.

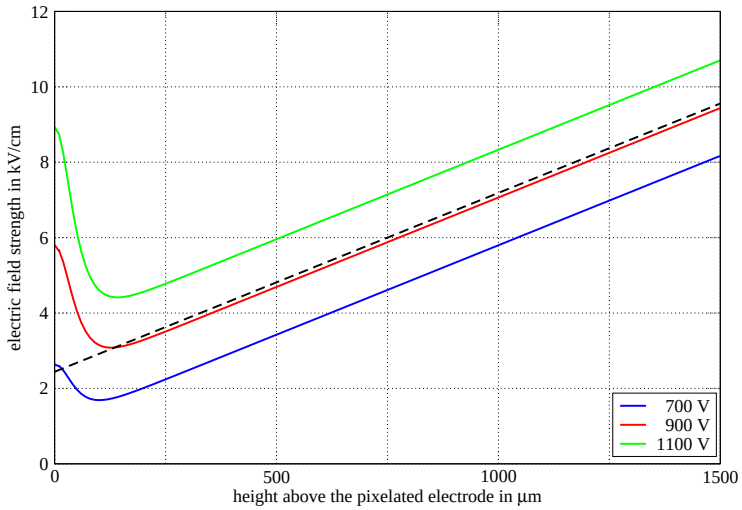

Figure 3.2 Electric field strength above the centre of the pixel for three different bias voltages (solid lines; 700 V, 900 V and 1100 V) and for a continuously contacted sensor surface, i.e. a plate capacitor like setup (dashed line; bias 900 V).

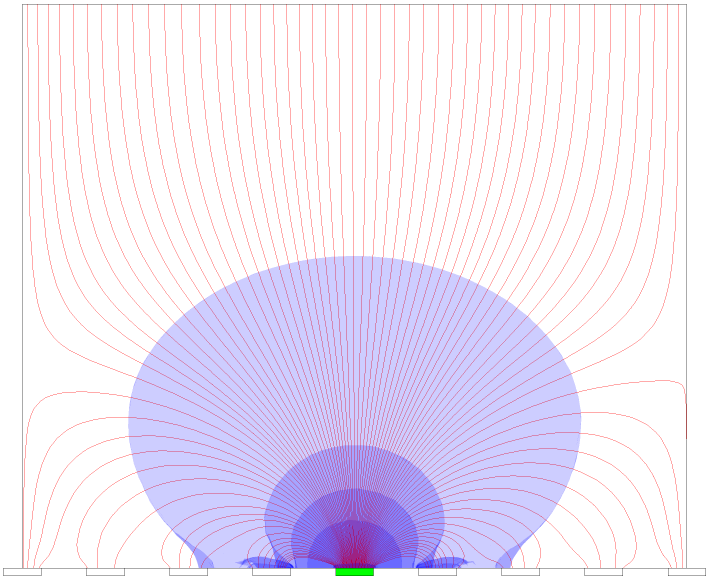

Figure 3.3 Weighting field lines (red) and weighting potential (blue shaded area) of the central electrode (green) for the standard setup calculated in 3D. The light blue area indicates the 1% surface of the weighting potential, the subsequent steps are 5%, 10% and 20%. The small disturbance close to the neighbouring electrodes has numerical origin and is due to the 3D overlay. The main signal induction process takes place directly above the electrode, but the induced signal rises straight at the beginning of the motion.

potential starts to bend. As the two boundaries have defined values, i.e. zero and one, the only way to change the slope is to sag between the two points.
For the standard setup, the weighting potential and weighting field is plotted in figure 3.3. The lower electrode is pixelated, the electrode of interest is in the centre. The clear difference to the actual electric field inside the material as in figure 3.1 is clearly visible. The weighting potential reaches into the neighbouring pixel volume, which leads to induced signals on the electrode even if the charge is drifting only in the neighbouring pixel volume. In figure 3.4, the weighting potential is plotted as a function of the distance to the pixelated surface. The weighting potential is a function of the ratio between the sensor thickness, the electrode and the pixel size, hence the amount of parameters is reduced by one.

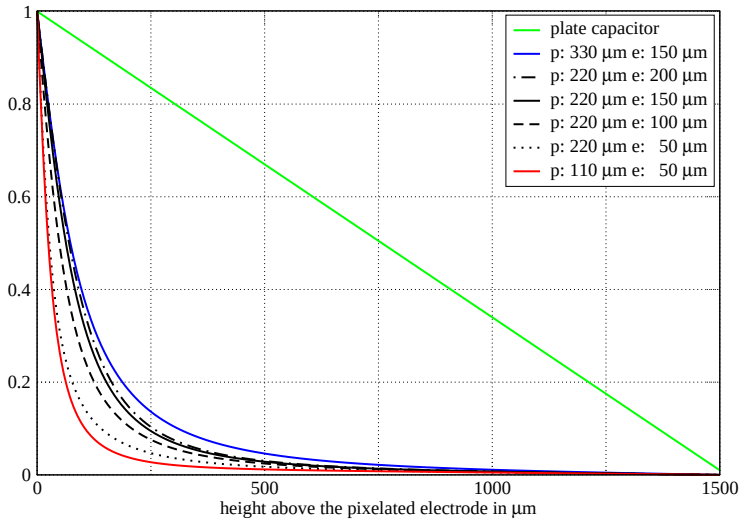

Figure 3.4 Weighting potential above the centre of the pixel for different pixel sizes (solid lines), different electrode sizes (dashed lines) and for a homogeneously contacted material, i.e. a plate capacitor (solid line).

3.2 Currents and Collected Charges

The bias voltage, which is applied across the sensor layer, accelerates the selected free charges inside the material towards the collecting pixelated electrode. The opposite charge carriers drift to the opposite homogeneous electrode and only have a very small influence on the signal shape. The charge selection is done by the polarity of the bias voltage, but in the case of CdTe and the aim to measure fast signals, the only reasonable choice is to collect electrons.
The signal induction process on the electrodes takes place during any motion of the charges. In the case of a plate capacitor, a continuous motion in the drift direction, i.e. from one side of the sensor layer to the other, leads to a constant signal on the electrodes, as the weighting field has a constant value. Inside a plate capacitor-like setup of a doped sensor layer, the weighting field is a constant, but the charge motion is a function of the distance towards the electrode. In figure 3.5, the signals generated by electron clouds starting at different heights above the electrode are plotted. As electrons and holes are generated at the same location, but drift in opposite directions, the signals will be superimposed. The slope of the signal depends on the drift speed of the charges. In CdTe, the electrons are ten times faster then the holes, which results in very small current signals from the holes. As the ratio between the summed electron and hole signal only depends on the initial distance towards the collecting electrode (z-direction), the z-position can be reconstructed from the signal. But on the other hand, no information about the lateral position (x-y-direction) is available.
If one side is pixelated, the lateral position can be obtained as each electrode measures a different induced signal. A charge cloud starting far away from the pixelated electrodes induces mirror charges on multiple electrodes, but as the charge cloud gets closer to the pixelated surface, the mirror charges move towards the electrode directly below the charge

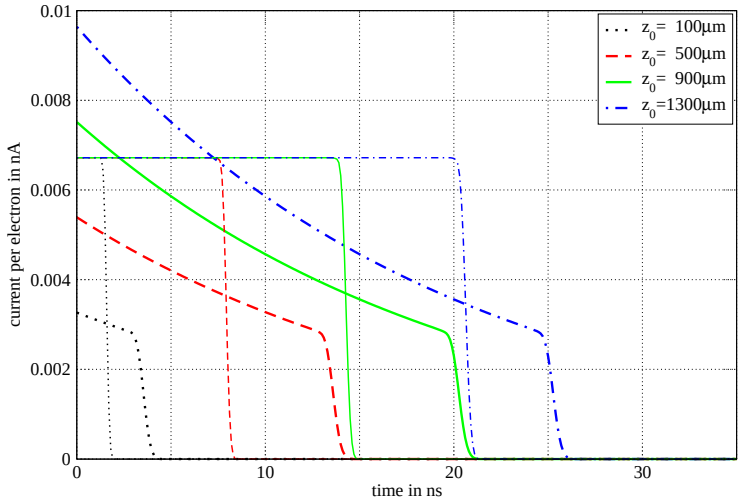

Figure 3.5 Electron signals inside a plate capacitor-like setup. The thick lines represent the doped case, whereas the thin lines correspond to the undoped case. The doping leads to longer drift times and to a change in the drift velocity as a function of position.

cloud. In the moment the charge cloud arrives at a single electrode, the charge and the mirror charges eliminate each other, i.e. the signal generation for this charge cloud is finished. As different pixelated electrodes all show a similar behaviour when the charge cloud is far away, but react differently when the charge cloud is approaching the pixelated surface, the signal is induced mainly close to the electrodes. The increase in lateral position information is compensated by the loss of the information about the distance towards the surface.
The z-direction can be reconstructed by measuring the fraction of the charge cloud which is collected on the electrode. The maximum fraction of the charge cloud is equal to the weighting potential difference from the starting point of the motion to the electrode. This is only possible if the charge cloud consists of only one charge type and the exact number of charges in the cloud is known. In the case of X-ray absorption, the charge cloud generated by the interaction is made of both charges which will drift in opposite direction. The different drift directions and the different charges lead to a signal with the same polarity. The sum over both signals will lead to a complete charge collection if no charges are lost due to recombination, trapping or charge sharing. Additionally, the number of generated charges is not known in a real measurement.
In figure 3.6, the results of signal measurements are shown for a 1600 μm thick CdTe sensor with 220 μm pixel pitch and 195 μm electrode size. The measurements have been carried out using a ^{60}Co source. The X-ray photons interacted with the CdTe sensor and the induced signals on the electrodes were measured with an oscilloscope [27]. This results in a superposition of pulses from any interaction point inside the material, hence the exact timing and pulse dimensions cannot be extracted from the measurement. But the pulse can be analysed by its shape: the signals are asymmetric which is a proof for the induction process.
The signal width is in the order of 7 ns (full width half maximum) and the variety between the pulses is very large. The pulse width can be explained by two effects: the doping pro-

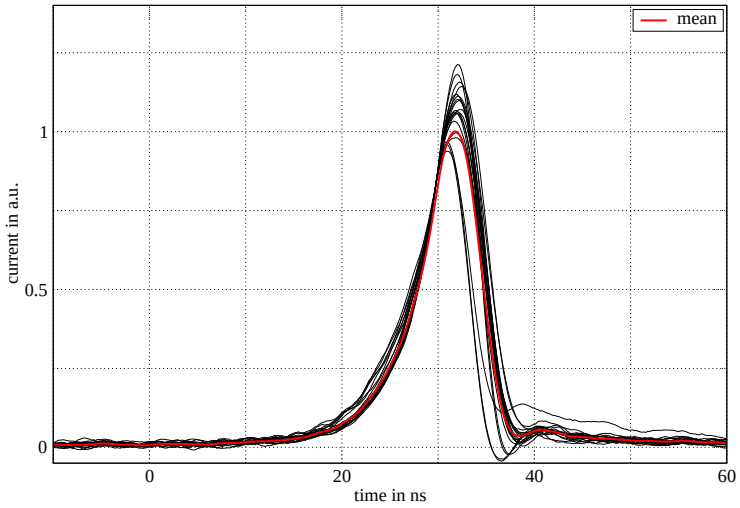

Figure 3.6 Measurement of time resolved signals for homogeneous irradiation of a pixelated CdTe sensor with ^{57}Co source, i.e. photons with monoenergetic energies of 122 keV. The signals are amplified and measured with an oszilloscope. The black lines stand for individual pixels averaged over a hundred pulses. The red line shows the average over the pixel pulses. The large variety is due to the inhomogeneity of the material and the uncertainty of the interaction point due to the homogeneous irradiation.

file in the material used for the measurement leads to pulses which are 4 to 5 ns wide and the readout electronics add another 1 to 2 ns. The large variety of the pulses is due to the homogeneous irradiation of the material which leads to interaction points centrally in the pixel, but also close to the pixel edge and even in the neighbouring pixel cells. The discrimination of the pulse heights can be applied to select the central interaction points. The resulting pulses can be averaged to reduce statistical fluctuations.
Due to the induction process, the signal is generated on the electrodes before the charge cloud touches the electrode. The motion of the mirror charges on the electrodes leads to the main signal in the electrodes when the distance between the charge cloud and the electrode is very small. When the charge cloud actually penetrates the electrode, the number of charges in the volume is decreasing, and the signal strength is also decreasing as the induction is a product of the weighting potential and the flux, i.e. the concentration and the velocity.
In figure 3.7, the electron signal of charge clouds at different starting heights is plotted as a function of time. The different signal shape and timing for the doped and undoped material are shown. The doping leads to a slower drift near the collecting electrode which leads to a lower and broader current signal. But even the timing structure changes: in the undoped case, the signals are equally spaced in time as the starting points were equally separated in space; but in the doped case, the drift speed varies as a function of the height above the elecrode. This leads to shorter time differences between the signals which start further away from the electrode. Additionally, the current pulses are very homogeneuos in the doped case, as any charge cloud is inducing the main signal in a small area, where the drift speed is relatively small and therefore the broadening due to diffusion does not have a strong influence. In the undoped material, the maximum height of the current

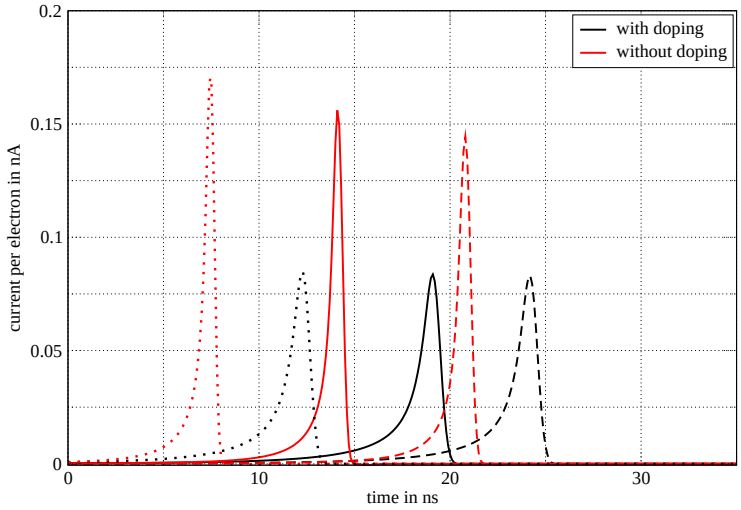

Figure 3.7 Electron signal for charge cloud starting points in the middle above the electrode. Three starting heights are plotted: 500 μm (dotted lines), 900 μm (solid lines) and 1500 μm (dashed lines). The signals in the doped material (black) are building up later than in the undoped material (red). As the induced charge is the same, the signals in the doped material are wider.

signals is decreasing with increasing drift time due to the increasing cloud radius.
As mentioned above, the charge cloud induces mirror charges on more than one electrode. The mirror charges move during the motion of the charge cloud and induce a signal on the electrodes. When the charge cloud is far away from the pixelated electrodes, the electrodes in an area around the projection of the charge cloud will all measure an equal signal. This will be true for most of the motion, but when the charge cloud gets close to the pixelated surface, the signals differ. If the charge cloud starts above the centre of a pixel, the central signal is rising and going back to zero. The signal on the neighbouring electrode starts rising like the central signal, but is not reaching the maximum value as the signal is superimposed with a negative signal which leads to a compensation of the collected charge as no part of the charge cloud reaches the electrode.
Electrodes which are further away from the starting point of the charge cloud also measure an induced signal, but the signal varies from the central one a lot earlier and the compensating negative signal is smaller. Hence the amount of charge induced on the electrodes is even smaller than in the neighbouring electrodes and will also vanish in the end as no charge is collected. In figure 3.8, the signals for the central, the directly neighbouring and the diagonal pixel electrode are plotted.

3.2.1 Different Bias Voltages

The bias voltage can be altered in a range which depends on the material. On the one hand, the sensor layer needs to be depleted to react like an active material, on the other hand, the applied voltage must not be too high to avoid electric breakdown. The drift velocity of the charges directly depends on the electric field inside the volume. In figure 3.9

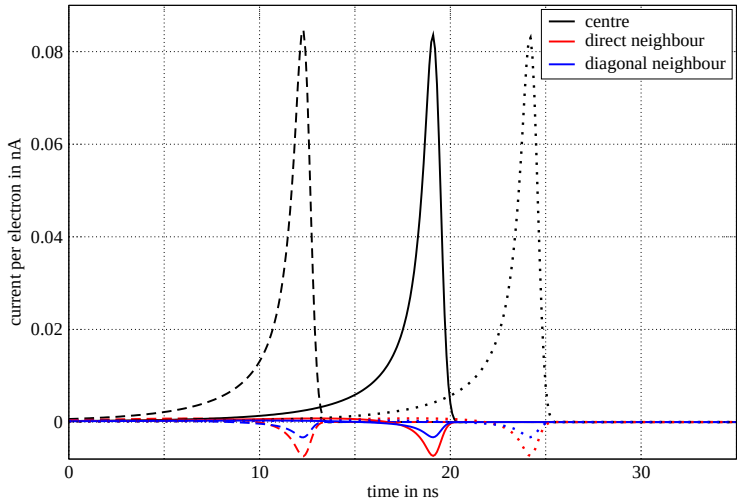

Figure 3.8 Electron signals for the central pixel, the adjacent pixel and the diagonal neighbouring pixel. The two sets of signals are for 500 μm (dashed lines), 900 μm (solid lines) and 1300 μm (dotted lines).

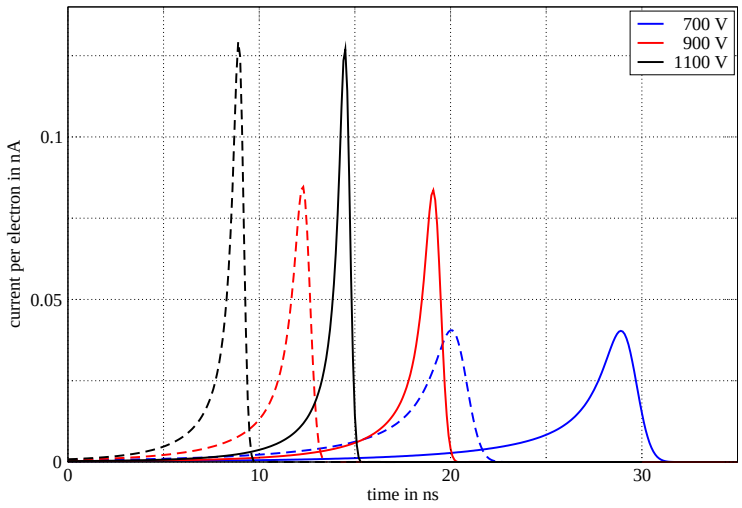

Figure 3.9 Electron signals for charge clouds starting at 500 μm (dashed lines) and 900 μm (solid lines) above the centre of the collecting electrode. The three different line pairs are for three different bias voltages (700 V, 900 V and 1100 V).

the signal of a spherical charge cloud starting centrally above the collecting electrode is plotted for different bias voltages. Larger bias voltage leads to faster charge cloud motion and hence to shorter drift times. The end of the signal is shifted linearly due to the change of the drift time, but the beginning of the signal cannot be taken as a measure as the signal starts immediately with the interaction of the X-ray.

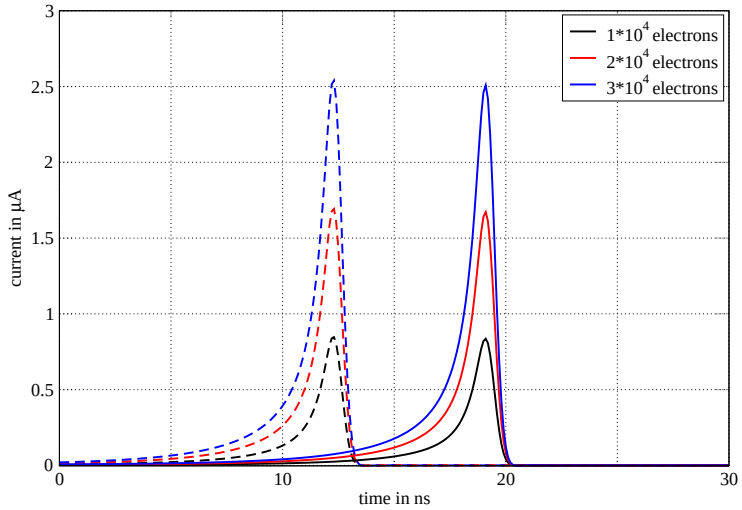

Figure 3.10 Electron signals for charge clouds starting at 500 μm (dashed lines) and 900 μm (solid lines) above the centre of the collecting electrode. The three different lines are for three different integrated charge amounts.

3.2.2 Different Initial Charge

The initial charge distribution can have different sizes, different positions and different amounts of charge. The effects of these possible changes in the initial conditions will be evaluated in the following part.

Amount of Charge

The amount of charge inside the initial distribution can be modelled by summing up the contributions of single charges. This results in the simple scaling of the signal due to the amount of charges. In figure 3.10 the signals for three different values of the integrated inital charge are plotted. The direct linear behaviour of the signal to the amount of charge leads to the opportunity to normalise the signals to a unit charge and just scale the signal to the charge inside a simulated charge cloud.

Size

The shape of the initial charge cloud is modelled as a sphere which has smooth boundaries to avoid unphysical diffusion. The size of the sphere can be scaled, which leads to different shapes of the induced signal. In figure 3.11 signals for three different diameters of the initial charge cloud are plotted. The charge cloud motion starts above the centre of the collecting electrode. The effect of an anisotropic change of the diameter to model the inner electrostatic repulsion of the charge cloud can be implemented in the simulation. As the difference between the three different charge cloud diameters is rarely visible within the standard setup (see figure 3.11), the change of the signal due to repulsion is even smaller.

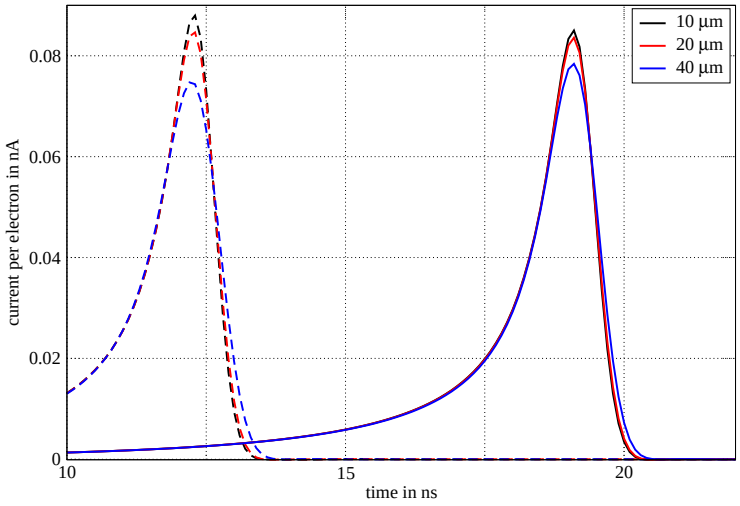

Figure 3.11 Electron signals for charge clouds starting at 500 μm (dashed lines) and 900 μm (solid lines) above the centre of the collecting electrode. The three different lines are for three different charge cloud sizes. In the legend, the radius r_0 is given and the time axis is expanded for better visibility.

Different Interaction Depth

X-rays penetrating the sensor material are attenuated slowly within the sensor volume. Due to this, any interaction depth can occur in the absorption process. The signals which are induced on the electrodes show a strong dependency on the z-position, i.e. the interaction depth: with increasing interaction depth the time till the signal rises to its maximum is shortening as the travelling distance is decreasing, and the amount of induced charge is decreasing due to the weighting potential. In the lefthand side of figure 3.12, the electron current signals of charge clouds from different starting heights above the pixelated surface are shown. The time gaps between the current signals are not equal in size although the distances of the initial charge clouds were exactly the same. This is due to the slope of the electric field hiwch leads to a varying electric field strength and hence a varying speed of the charges as a function of the z-position. The signals can be integrated over time and by doing this the induced charge on the electrode as a function of time can be acquired. On the righthand side of figure 3.12 the induced charge for different starting heights above the pixelated surface is plotted. The maximum level of the induced charge is a function of the starting height, as the weighting potential defines the fraction of the signal which comes from the electrons. The remaining fraction of the charge would be subject to the holes, but as the holes are very slow moving inside the material, the promient charge pulse is coming from the electrons. The charge pulse will rise slowly to the maximum available charge after the electron pulse is finished. However, parts of the charges may be lost due to trapping and recombination.

Relative Lateral Position

The signal also changes its shape depending on the position inside the pixel. The relative position to the centre has a main influence on the signal, even if the distance to the

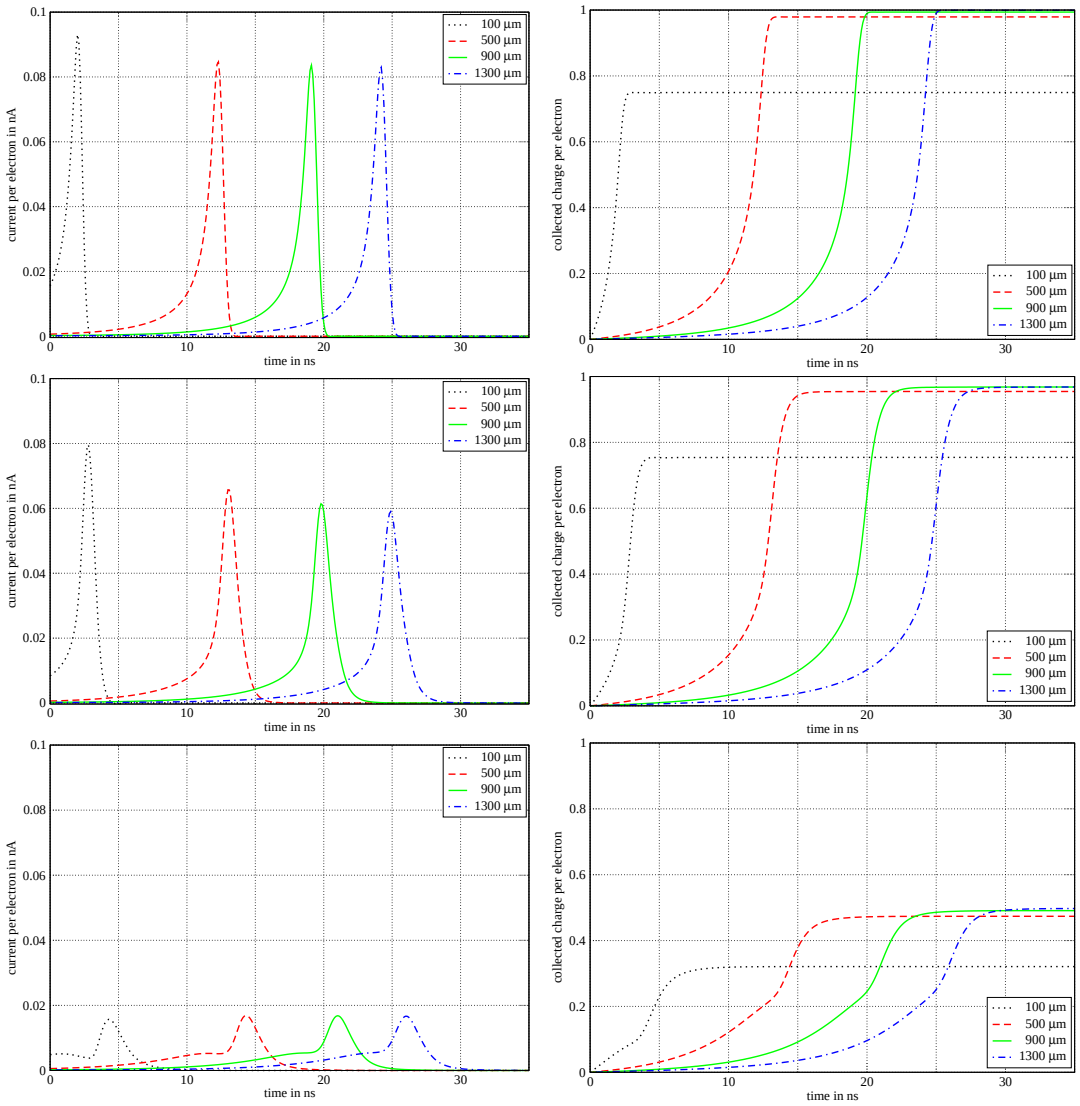

Figure 3.12 Electron signals for different starting positions. There are four different z-positons in each plot as labelled in the legends. Each row corresponds to a different lateral position (top: central, middle: close to the pixel edge, bottom: directly above the pixel edge). Left column: induced currents on the central electrode for different starting points. Right column: collected charges for the same starting points.

pixelated surface is the same. Charge clouds which start close to the edges of the pixel deposit parts of the charge in the neighbouring pixel, which is then missing in the central signal. But even if all the charge is collected inside the central pixel, the shape of the signal can vary due to the subpixel position. As the charges may have to travel a longer distance to the electrode, the signal is getting broader.
In figure 3.12 the effect of different subpixelpositions is shown. Each row corresponds to a specific position. In the top row, the charge cloud starts at positions on the central axis of the pixel and the z-position is set as labelled in the plot. For the bottom row, the charge cloud was set directly above the pixel edge, i.e. the x-position is 110 μm. In the middle, the starting points vary along a line which is close to the pixel edge, i.e. y-position is set to the origin, the x-position is set to 80 μm (which is in the area of the pixel where no electrode is straight beneath).

3.2.3 Different Pixel Pitch

The pixel pitch has influence on the possible spatial resolution of the detector. Depending on the thickness of the sensor layer, the pixel pitch can be varied in a range which is limited by two aspects: too large pixels will lead to a loss of spatial resolution and in a loss of the prominent signal shape; too small pixels suffer from charge sharing due to diffusion and will therefore not result in a higher spatial resolution.
Additionally, small aspect ratios between the pixel pitch and the sensor thickness lead to strongly bent weighting potentials which results in small areas of strong induction. Charges have to move into the area where most of the induction takes place to generate a signal on the electrode. In figure 3.13, the signals for different pixel pitches are plotted. The electrode size scales with the pixel pitch. The signal shape varies significantly due to the change of the weighting potential. Smaller pixel pitches lead to sharper signals, but also give rise to the case where charge clouds reach into neighbouring pixels.

3.2.4 Different Pixel Electrodes

In real setups, the pixel electrodes cannot have equal dimensions as the pixel pitch. The area between the electrodes is needed to separate the electrodes from each other. This leads to the option to vary the electrode shape and dimension. The effect of different electrode dimensions on the signal shape is plotted in figure 3.14. The geometrical design of the electrodes has only minor influence on the signal shape as long as it is not different for the two main directions of the pixel grid.

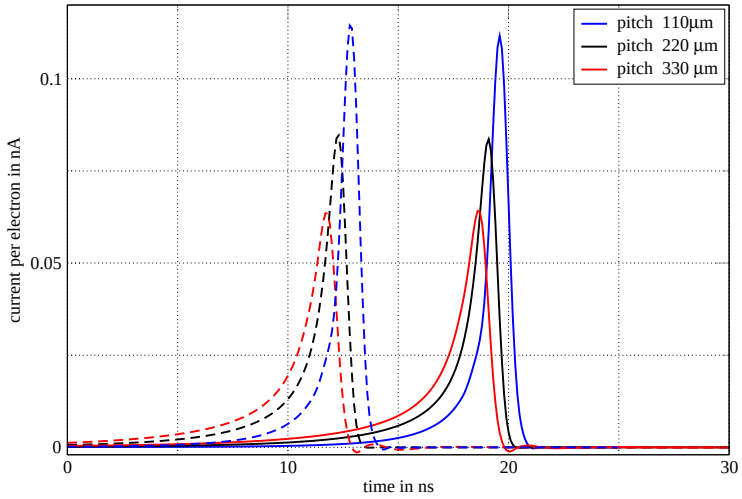

Figure 3.13 Electron signals for charge clouds starting at 500 μm (dashed lines) and 900 μm (solid lines) above the collecting electrode. The different lines show the signals for different pixel pitches. The electrode sizes are scaled with the pixel pitch.

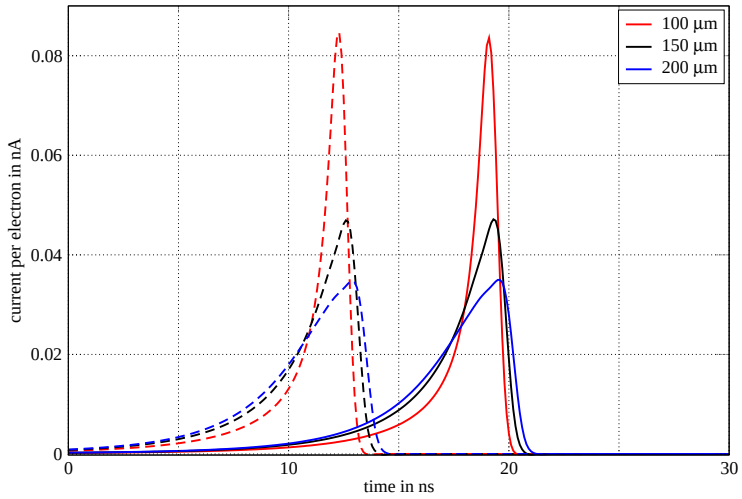

Figure 3.14 Electron signals for charge clouds starting at 500 μm (dashed lines) and 900 μm (solid lines) above the collecting electrode. The different lines show the signals for different electrode sizes where the pixel pitch is kept constant at 220 μm.

3.3 Steering Grid Geometry

The signals which enter the electronics behind the sensor layer are required to be short to allow the detection of single events even for high rates. As shown in section 3.2, the signal width can be altered by different aproaches: increase of the bias voltage, reduction of the pixel size and reduction of the electrode size. But, the bias voltage which can be applied is limited as the current across the sensor increases with increasing bias voltage and higher bias voltage also cause difficulties in the vicinity of the sensor due to electric breakdown through air.
Smaller pixels suffer strongly from charge sharing as the initial charge cloud size is depending on the initial interaction in the sensor. If the pixel cells are in the size of the inital charge cloud, the charge will allways be collected in several pixels. This can be used to increase the spatial resolution by applying a centre of gravity readout, but the possible event rate is decreasing. Smaller electrodes in sufficiently large pixel cells lead to short signals, but the signal shape is depending strongly on the lateral position of the starting

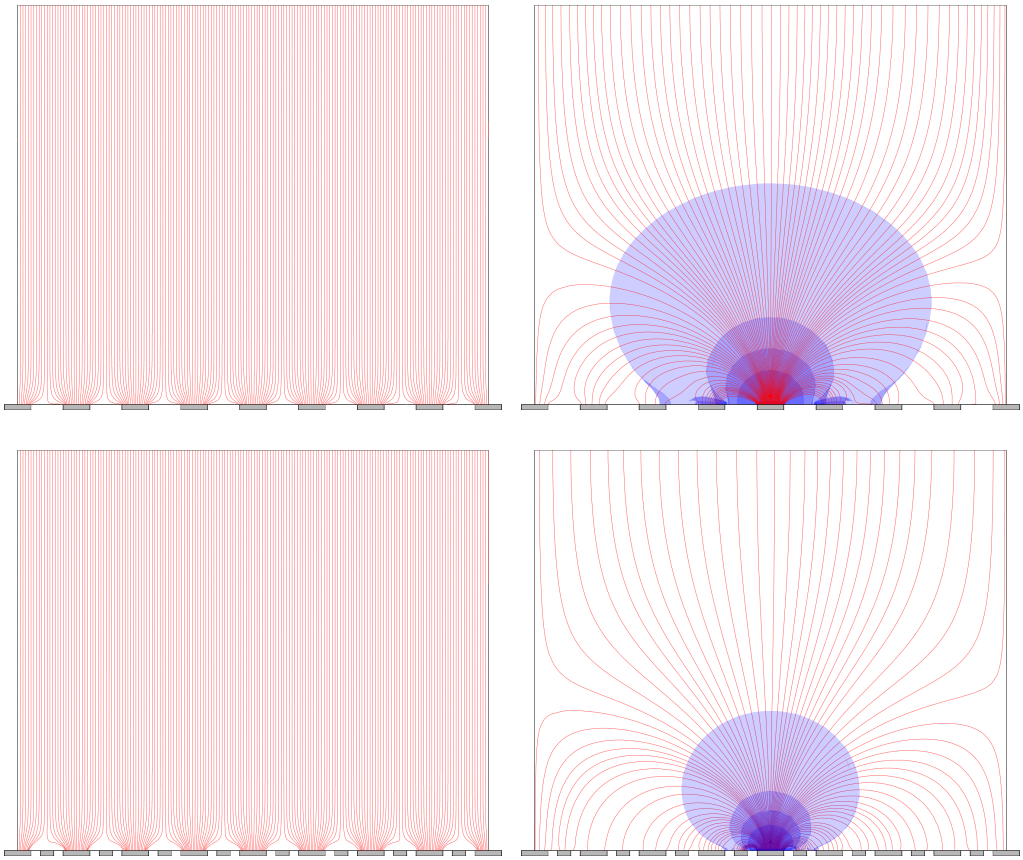

Figure 3.15 Streamline plot of the electric bias fields (left column) and weighting fields (right column) for the geometry without (top row) and with (bottom row) steering grid. The bias voltage is set to 900 V and the steering grid voltage is set to 50 V. In the weighting field images, the weighting potentials are included as shaded areas (values (large to small area): 1%, 5%, 10% and 20%).

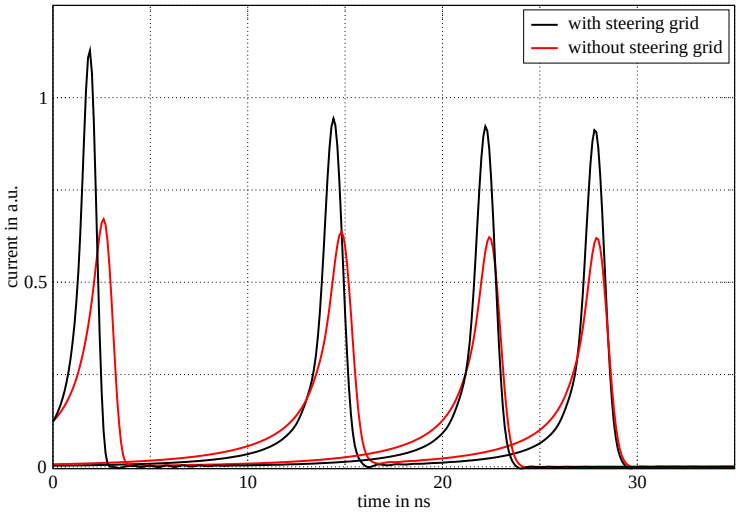

Figure 3.16 Electron signals for charge clouds starting at 100 μm, 500 μm, 900 μm and 1300 μm centrally above the collecting electrode. The red lines show the signals without a steering electrode and the black lines correspond to the geometry with a steering grid.

point of the charge cloud.
An alternative way to shorten the signals is the modification of the geometry by applying an additional set of electrodes to shape the electric and weighting potential. The so-called steering electrode is positioned as a grid between the signal collecting electrodes and a voltage is applied to repell the collected charges from the area between the electrodes. When electrons are collected as in the case of CdTe and the aim of quick detection, a positive potential is set on the steering electrode.
In figure 3.15, the electric and weighting fields are plotted to show the effect of the steering grid on the fields. The electric field is only modified very close to the collecting electrodes at the bottom. Electric field lines and hence the charges which move according to the electric field are directed to the collecting electrode without moving close to the surface of the sensor between the electrodes. The electric field strength and hence the drift speed of the charges is increased close to the electrode which leads to shorter signals.
Additionally, the weighting potential is changed. The region of high weighting potential values, i.e. the region of high induction, is getting smaller as more electrodes are present close to the collecting electrode. In the right part of figure 3.15, the reduction of the high induction region is shown.
In figure 3.16, the induced electron signals for charge clouds starting at different heights centrally above the collecting electrode. The two sets of signals correspond to the same pixel and electrode dimensions. But the signals for geometry where the steering grid is applied are narrower and higher as the area below the curve, i.e. the collected charge, is the same.

4 Summary and Discussion of Part I

The calculation of the electric potential and its gradient, i.e. the electric field, can be performed in a rather direct way as the shape of the potential is repeating in each single pixel cell. This repetition leads to ideal symmetry conditions which dictate the boundary conditions which have to be applied. The doping of the material is implemented as a space charge density. The density can be extracted from electric field measurements. This leads to the option to implement not only homogeneous doping, but also spacially varying doping profiles. In combination, the doping and the clear symmetry lead to very good results of the electric field calculation, which is shown in figures 3.1 and 3.2.

The weighting potential calculation suffers from the fundamental restriction of the simulation volume while the potential is extending to infinity. However, the systematic error which results from the finite size of the simulation volume can be neglected if the simulation takes a sufficient large number of neighbouring electrodes into account. The change of the potential in the central pixel cell which is observed in the signal induction process is diminishing when more neighbouring electrodes are added and so the weighting potential is almost reaching its final shape. The simulation takes four neighbouring pixel cells in all four directions into account which results in a 9x9 pixel simulation area. This leads to a good agreement with the final shape within a reasonable memory and computing time consumption.

The currents which are induced on the electrodes originate in the motion of the mirror charges. The simple case of a plate capacitor setup can be observed for clarity. An electron cloud starting in the middle of the sensor and moving to the positive electrode induces a constant signal during its motion as the electric and the weighting potential have the same shape. As electrons and holes are generated in pairs by the interaction of X-rays with the sensor, the holes will drift in the opposite direction. The drift will be slower due to a smaller mobility of the holes, but the induced signal will have the same sign, as the motion direction and the charge sign are both changed. In figure 3.5, only the electron signal is plotted. The hole signal would be added to the electron signal which leads to an additional step in the graph. The timing of the two steps depends on the z-position of the starting position, but the relative signal height is due to the ratio between the mobilities of electrons and holes.
Doping of the sensor material leads to an inhomogeneous electric field strength and hence an inhomogeneous drift velocity. The collected charge on the electrode depends on the z-position of the starting point, but as the current is the product of the the charge velocity and the weighting field, the signal shape will not be a constant, but tilted as shown in figure 3.5.
If the collecting electrode is pixelated, the shape of the signal changes. The induction process is not independant of the z-position in the sensor, but has a maximum close to

the collecting electrode. The weighting field maximum close to the collecting electrode leads to the main signal induction close to the electrode. The motion of the charge cloud at larger distances has only minor influence on the signal. Therefore, the hole motion loses impact on the generated signal. For this reason, the hole motion is neglected in the following simulation.

As in the plate capacitor geometry, the doping of the material has a strong influence on the signal. In the evaluated geometry, n-type material leads to slower motion on the charges close to the collecting electrode. Thus, the signal is building up later and is getting wider, as shown in figure 3.7. As the collected charge is the same, the signal height is decreased. Additionally, the signal height is varying less with the z-position of the starting point as the diffusion is not affecting the temporal shape of the signal as much as the slowing down of the drift velocity by the doping.
The pulse shape was investigated with respect to different parameters. The bias voltage regulates the electric field strength inside the material. As the drift motion is directly coupled to the electric field by the mobility, the pulses change with the bias voltage. Higher bias voltages lead to shorter drift times and to sharper signals which can be observed in figure 3.9. The number of electrons in the charge cloud only results in a higher signal, but the signal shape is not changing.
The lateral position inside the pixel cell has some influence on the signal shape (see figure 3.12): starting points at the center of the pixel above the electrode induce a strong and sharp signal as the motion of the charge cloud is direct. If the charge cloud starts closer to the pixel edge, some charge may drift or diffuse in the neighbouring pixel which leads to a loss of signal in the central pixel. But even starting points where the whole charge is collected by the central electrode can have smaller and wider signals. If the charge motion is not perpendicular to the electrode surface but has to drift sideways to arrive at the electrode, the current pulse will be wider due to the elongated drift way close to the collecting electrode.
This drift way elongation depends on the ratio of the pixel pitch and the electrode size. Smaller electrodes cover less of the pixel area and hence more lateral drift is necessary to reach the electrode. Additionally, the area of strong weighting potential gradients is getting smaller when the electrodes are decreasing in size (see figure 3.4). Smaller electrodes and smaller pixel pitches both lead to sharper signals, but the spatial resolution of the detector cannot be improved without limit. The main reason is the distribution of the signal to more than one electrode (charge sharing). This is obvious for charge clouds which are larger than one pixel cell as some of the charge will drift to the neighbouring electrode. But even when the charge cloud is smaller than the pixel size, a temporal signal will be induced on the neighbouring electrode.

The simulation offers a good access to the spatial distribution of the induced currents which can help to design future detector geometries. The knowledge of the timing structure of the signals allows the optimisation of the geometry as well as the readout electronics behind the sensor layer.

Part II

Radiation Field of a Medical Linear Accelerator

5 Basics of Medical Irradiation

Medical irradiation is a commonly used treatment method for tumour diseases. The basis for this treatment is the different response of healthy and tumour tissue to exposure with ionising radiation. Healthy cells can cope with radiation damage of the DNA more efficiently than tumour cells. This leads to different survival rates of the different tissues thus to the possibility to injure or destroy tumour cells (i.e. to force the cells to apoptosis) while keeping healthy cells alive.

5.1 Dose Definition

The effect of ionizing radiation on material depends on the type of radiation, the energy and the material itself. Consequently, there are different definitions to characterize the ionizing effect. The following list explaines the most commonly used [28]:

1. *Kerma* (only photons): The Kinetic Energy Released in MAtter takes account of the kinetic energy of all charged particles generated by non-charged particles interacting with the material. These charged particles deposit energy in further interactions with the material, but these secondary processes do not contribute to the kerma K:

$$K = \frac{\delta E_{kin}}{\delta m} \tag{5.1}$$

   The unit of kerma is $Gray(Gy) = \frac{J}{kg}$. This measure can only be applied to uncharged particles like photons. The *air kerma* is the kerma of photons in air, which can be obtained at standardized conditions with the help of ionisation chambers.

2. *Absorbed Energy Dose*: The complete energy δE_{abs} deposited in material of mass δm by incoming ionizing radiation is described by the absorbed energy dose:

$$D = \frac{\delta E_{abs}}{\delta m} \tag{5.2}$$

   The unit of the absorbed energy dose is $Gray(Gy) = \frac{J}{kg}$, which is equal to the unit of kerma. But in this case, the transfer of energy from the charged particles to the material is also taken into account.

3. *Dose Equivalent*: Different types of radiations have different biological effects. The dose equivalent H equals the absorbed dose, but is weighted with a quality factor f_Q (see table 5.1) to take the biological effects into account.

$$H = f_Q \cdot D = f_Q \cdot \frac{\delta E_{abs}}{\delta m} \tag{5.3}$$

   The resulting unit is $Sievert(Sv) = [f_Q] \cdot Gy = Gy$. As the quality factor has no unit, it is the same as for the absorbed energy dose.

These main dose definitions are followed by further definitions which also describe the energy deposition by ionising radiation. In some cases, the definition is even based on specific applications like computed tomography: *CTDI* - "Computerized Tomographic Dose Index" [29].

Table 5.1 Quality factors for different sorts of radiation. The distribution of energy deposition varies between the different sorts of radiation. The damage done to the cell's DNA can be repaired by damage control mechanisms, but depend on the rate the damages are induced. The definition of the quality factor is based on the linear energy transfer, which is a measure of the ionising density.

Radiation	Quality Factor f_Q
photons, electrons	1
neutrons	5-20 (depending on the energy)
protons	2
alpha particles, heavy nuclei	20

5.2 Tumour Treatment

The treatment of tumours with radiation has to deposit the necessary dose in the tumour tissue, so the tumour cells get damaged enough to undergo the transition to apoptosis. Additionally, the healthy surrounding tissue needs to accumulate as little dose as possible to survive the treatment with little damage. The different cell types show a different response to the accumulated dose. An example of the cell survival rate is shown in figure 5.1. The moderate decrease of the cell survival rate is caused by the balance of the damages of the cells and the repair processes. The slopes vary for different tissues. This variation is due to the fact that the sensibility of the cells to irradiation is a function of the cell cycle. As tumour cells have an increased metabolism and grow quickly, the cell division is performed quicker and more often. Therefore, the tumour cells lose parts of the ability to repair damages which occur to the DNA. This leads to an increased rate of irreparable errors in the daughter cells which may then not be viable.
The cell survival rate as a function of the deposited dose can be described by the linear quadratic model:

$$\text{cell survival rate}\,(D) = e^{-(\alpha D + \beta D^2)} \tag{5.4}$$

where D is the applied dose and α and β are coefficients which describe the process of the cell survival rate. The value of α dominates the low dose region, whereas the β is dominant for high applied dose. The amount of dose where both effects have the same impact is decribed by the $\frac{\alpha}{\beta} - value$. This differs for different types of tissue as can be seen in table 5.2, which gives an impression of the sensibility of a tissue to irradiation. Higher values for the $\frac{\alpha}{\beta} - value$ correspond to a quicker response to irradiation. At low doses, typically below $1\,Gy$, a fast decrease of the cell survival can be observed caused by the need of a certain level of cell damage to stimulate the repair processes in the cell. This discrepancy to the linear-quadratic model is called *low-dose hyperradiosensitivity* [30]. When the dose is increased further, the cells show a recovery, the so called

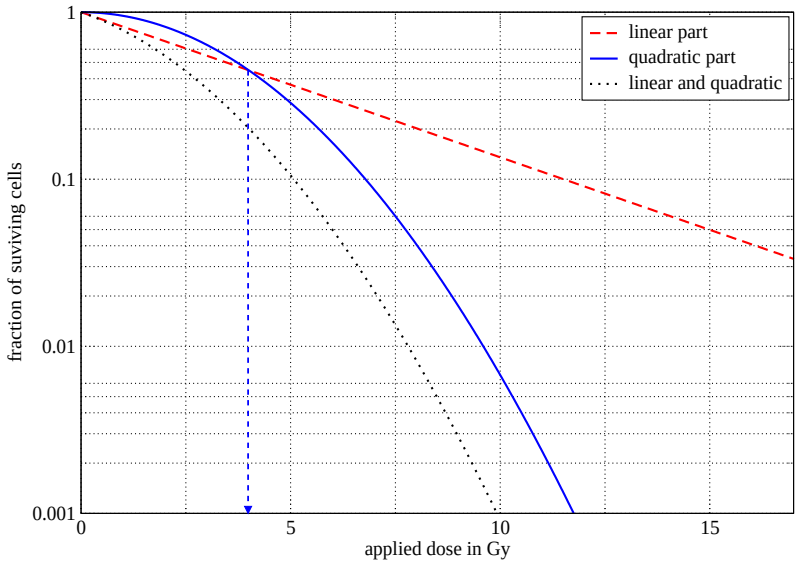

Figure 5.1 Cell survival rates for lung tissue. The cell survival rate is plotted against the accumulated dose. The dose where α and β have equal impact is marked by the arrow.

Table 5.2 The amount of dose where the effect due to the linear and the quadratic impact are equal are shown for different tissues. The larger the value the quicker the response to irradiation.[31]

Tissue	$\frac{\alpha}{\beta}$ in Gy
tumour	10-25
skin	9-19
liver	1.4-3.5
lung	2.5-6.3

induced radioresistance. The combination of these two low-dose effects leads to a good agreement of the linear-quadratic model for higher doses.
As the healthy cells would get damaged as well even when the tumour cells are not sufficiently irradiated, the dose needs to be applied to a strictly limited area. For this reason, the irradiation utilises different sorts of radiation. Only electron and photon irradiation will be discussed in this thesis, but for medical issues proton and heavy ion treatment are also used.
Additional to restrictions of the irradiation area to the tumour, the dose application can be optimised by taking advantage of the different irradiation responses of different cell types. The values of α and β vary for different tissue and the repair of cell damages is realised a lot more efficiently in healthy cells. The fractionation of the irradiation dose can help to allow the healthy tissue to recover almost completely and to harm the tumour cells efficiently. In figure 5.2 the effect of the fractionation is shown. The total dose which is needed to destroy the tumour tissue is larger than in the case where the dose is applied in one step, but the healthy tissue is harmed a lot less in the subsequent irradiation mode.
Another supporting factor is the Bystander effect [32]: even unirradiated cells show a re-

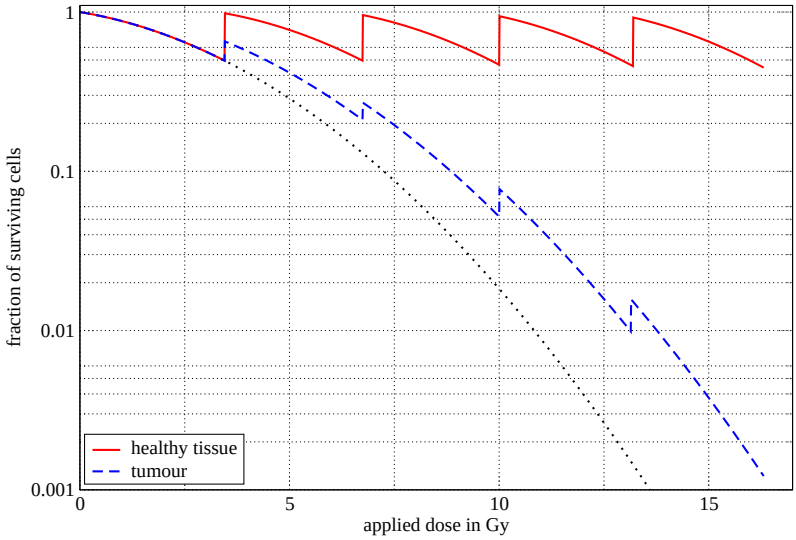

Figure 5.2 Survival rates of cells when irradiated as a function of applied dose. The dotted line corresponds to the irradiation on one step. If the applied dose is applied in fractions with several hours between the irradiation, the cells can repair some of the damages: healthy cells (solid line) can do this a lot more efficiently than tumour cells (dashed line).

sponse to the irradiation if the cells in close neighbourhood are forced to apoptosis by the irradiation. As more tumour cells will get damaged, this effect is more prominent in the tumour tissue.
Even if the dose is deposited only in the tumour volume, the accumulated dose inside the volume needs to be very different depending on the tumour. Leukemia (blood tumour) needs only 20 to 30 Gy to be treated sufficiently, but prostate and mamma cancer cells can survive even more than 50 Gy. Bone tumours and glioblastoma (brain tumour) can cope with doses above 70 Gy before being forced into apoptosis. This huge diversity needs to be part of the tumour treatment planning.

5.2.1 Photons vs. Electrons

Electrons and photons, though having the same biological weighting factor, show different behavior with respect to the penetration of material. The difference between the normalised depth dose distributions for different X-ray energies and for electrons can be seen in figure 5.3.
Photons interact with matter mainly by three effects: absorption, scattering and pair production [33]. These discrete steps occur during the passage of the photons through matter, but depending on the energy, the free path length between two interactions can be rather large. This energy-dependent attenuation leads to the possibility to use X-ray photons for different applications. Photons with energies above 30 keV can travel through the human body and can therefore be used for imaging as the attenuation of the photons also depends on the atomic number and the density of the material. The attenuation is described by the attenuation coefficient $\mu_k(E)$, where E is the energy and k stands for

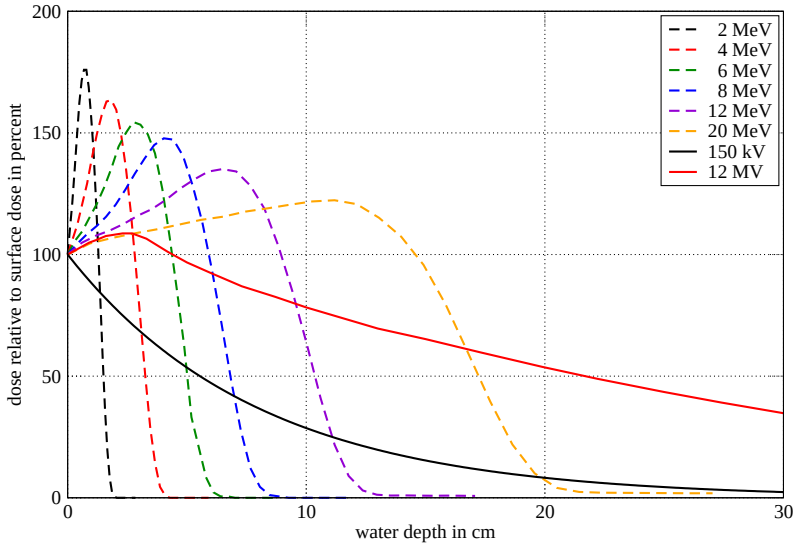

Figure 5.3 Qualitative depth dose distributions for electrons (dashed lines, [34, 35]) and for photons (solid lines, [36]) of different energies in water. The dose maximum is scaled to the surface for each graph. The dose distribution for the electrons has two components: the direct dose from electrons close to the surface and the component from generated Bremsstrahlung photons which reach deeper into the material. The photon depth dose distributions mainly show the attenuation and only a weak buildup effect for higher photon energies.

the material. The attenuation coefficient $\mu_k(E)$ is decreasing with increasing energy, except for certain material specific energies, where the energy rises above ionisation energy levels. As the detection of the X-ray photons is based on the same physical processes, medical imaging can only be performed with energies below 200 keV without increasing the applied dose due to the loss of photons in the detection.
Medical radiation treatment uses much higher energies up to 20 MeV, where the photons can pass through the matter more easily. The mean free path between two interactions is very long, thus the photons deposit energy in all depths of the human body. Additionally, the energy of the photons has to be transferred to electrons first to deposit energy in the volume. This leads to a buildup effect which reduces the surface dose, i.e. the dose in the skin. Photons can therefore be used to treat cancer cells inside the human body.
Electrons penetrate only very little into material in comparison to photons [37]. This reduced penetration depth is due to the different interaction processes, as the electrons are charged particles. Electrons transfer energy to the material by ionisation and excitation of the atoms. Additionally the electrons can lose energy by Bremsstrahlung. The ionisation and excitation of the atoms by scattering the bypassing electrons occurs very often at energies below a critical energy. Above this critical energy, the Bremsstrahlung is the prominent process for energy loss: electrons are decelerated in the Coulomb field of the atom nucleus and lose energy emitting a photon.
The penetration depth for electron energies used in medical irradiation is in the order of some centimeters. In contrast to photon irradiation, the dose distribution is not following an absorption law, but shows a buildup close to the surface, followed by a strong falling slope. Only photons generated through the interaction of electrons with the material will

penetrate into deeper regions of the human body. The energy deposition that is primarily close to the surface can be part of skin tumour treatment with only little effect on the inner organs.

5.2.2 Multifield Irradiation

Medical irradiation has to cope with two different goals: on the one hand, the tumour should be treated successfully and efficiently; on the other hand, the radiation protection of healthy tissue and sensitive organs even close to the tumour has to be kept under close observation. Irradiation plannig systems based on Monte-Carlo techniques can improve the applied dose distribution in the tissue by superimposing different irradiation fields from multiple directions [37].
As photon irradiation leads to a more or less homogeneous depth dose distribution, the superposition can be calculated like the simple back projection known from computed tomography. The regions of overlapping irradiation fields will experience an increase of the applied dose, whereas the surrounding tissue will only accumulate the dose from a single direction. Electron fields can be used to boost the applied dose close to the surface, even if the sensitive organs are in the irradiation direction.
As the treatment planning has to be performed for each patient and each tumour separately, treatment planning systems are optimised for short computing time. This is achieved by reducing the details of the simulation. This loss of accuracy is accepted as other parameters are not known exactly, like the response of the tumour cells to irradiation or the detailed beam shape and spectral distribution. Nevertheless, the simulation leads to a useful combination of irradiation directions and exposure times which can be transferred to the irradiation system and are used for tumour treatment. The increase of available computing power can be used to enhance the number of applied irradiation fields, which will improve the treatment planning. Additionally, the simulation can take more and more system and patient specific details into account to model the irradiation.

6 Simulation Setup

The simulation of the medical linear accelerator is build up to model particles passing through multiple geometrical components. The interactions with matter are based on physical processes which are implemented by cross section and probability functions in the Monte-Carlo simulation tool Geant4 [38, 39].
The simulations presented in this chapter were performed with the version 4.9.2.p01 including the data files for low energy electromagnetic processes version 6.2 [40]. The Monte-Carlo simulation tool Geant4 is developed within an international collaboration hosted at Cern. The complete source code can be downloaded for free [41]. In the following chapter, the parts of the simulation that were used are presented.

6.1 Basic Setup

The medical irradiation device consists of an accelerating unit for electrons, an energy selective bending magnet, a beam shaping collimation system and a homogenization system. For the electron irradiation, the electron beam is used directly, but for the photon mode, a transmission target is inserted to generate photons via Bremsstrahlung.
The electrons are accelerated in bunches inside the linear accelerator and leave the accelerator with a tuneable energy spectrum which reaches from some keV to the nominal maximum energy of the system. The maximum energy depends on the specifications of the system but normally reaches between 15 MeV and 25 MeV. An energy selective chromatically corrected bending magnet is attached to the accelerator. The bending magnet is tuned to a magnetic field strength to allow only electrons with a specific energy to pass through the exit collimator. As the magnetic field strength can be modulated from one irradiation to the next, the electron energy can be selected from the available spectrum. The bending magnet acts like a velocity filter for the electrons (Wien filter). Behind the energy selection, the electron beam is focussed onto the exit windows, where the simulation begins.
The electrons are directed towards the irradiation area and have an energy spread due to the selection out of a spectrum and due to the chromatic aberration of the bending magnet. The spectral uncertainty can be modelled by a Gaussian distribution with an energy dependent standard deviation. The size of the focal spot of the electron beam at the exit window is also modelled with a Gaussian distribution. Even non-circular distributions can be applied. The direction of the electrons, though pointing mainly towards the irradiation area (which is the z-direction by convention), is distributed according to a bivariante Gaussian model. A tilting angle is implemented to take account of a possible angular offset of the principal direction.
The electrons of the beam are propagated particle by particle by the Monte-Carlo simulation. The initial properties are determined using a random generator on the given distributions for the energy, the direction and the initial location. This directed but

divergent electron beam with a given energy spread is then propagated through the collimation system. In the case of photon irradiation, Bremsstrahlung photons are produced by the electron beam inside a target, which is also part of the simulation.
The beam is primarily collimated close behind the exit window by the primary collimator. This collimator differs in its shape depending on the irradiation mode. The main definition of the field size is realized by the x- and y-collimators. The y-collimation is performed by tilted lead blocks. The inclination of the main collimators, which depends on the opening, is to reduce the penumbra in the irradiation field. In figure 6.1(a) and 6.1(b), the inclination of the y-collimator is visible. The x-collimation is done by a multi leaf collimator: many thin lead leafs can be moved separately to form different irradiation fields. The tilting angle of the y-collimator cannot be implemented in each leaf for the x-direction, but the leafs are tilted in the y-direction to avoid radiation passing through the air gaps of the leafs. In the simulation, the leafs are modelled by lead blocks, as only square irradiation areas were studied.
As the applied dose needs to be controlled throughout the irradiation, a dose chamber is present in the beam - a dedicated one for each irradiation mode. The dose chamber is positioned between the source and the main collimation system.

6.2 Electron Irradiation

The penetration of electrons into material is strongly energy dependent and the dose distribution is localised close to the surface. Consequently, changes in the beam parameters significantly influence the applied dose in the illumination volume.
The standards for tumour treatment with electrons request a homogeneous flat illumination of the irradiation area. The slope on the edges of the illumination area, i.e. the penumbra of the electron field, is also part of the standards. Additionally, the pertubation of the electron beam with photons is restricted, as the penetration of the photons into deeper regions deposit dose in underlaying tissue. The beam is flattened and shaped behind the bending magnet, where the initial energy is selected. The nominal energy of the electron beam is defined through the depth dose profile, which leads to comparability of the electron beams even from different suppliers. A schematic drawing of the complete electron irradiation configuration is shown in figure 6.1(a).
The electron beam at the exit window of the magnet has dimensions of a few millimeters and is a pointlike source in comparison to the whole setup. Nevertheless, the exact shape and distribution of the electron beam is part of the simulation. A set of scattering foils is included to flatten the electron wave front and to enlarge the homogeneously illuminated area at the location of the patient. The beam is collimated to the requested illumination area at a later stage.
The electron dose distribution is monitored during irradiation with the help of an electron dose chamber. The dose chamber consists of several layers of ionisation chambers and is not intended to model the shape of the beam, but to allow the inspection of the electron flux. The dose is measured between the source and the collimation system.
The main collimation system is included in the medical linear accelerator head. As the distance from the x- and y- collimator to the patient position is quite large, the divergent electron beam is widening and the electrons are interacting with the surrounding air. This

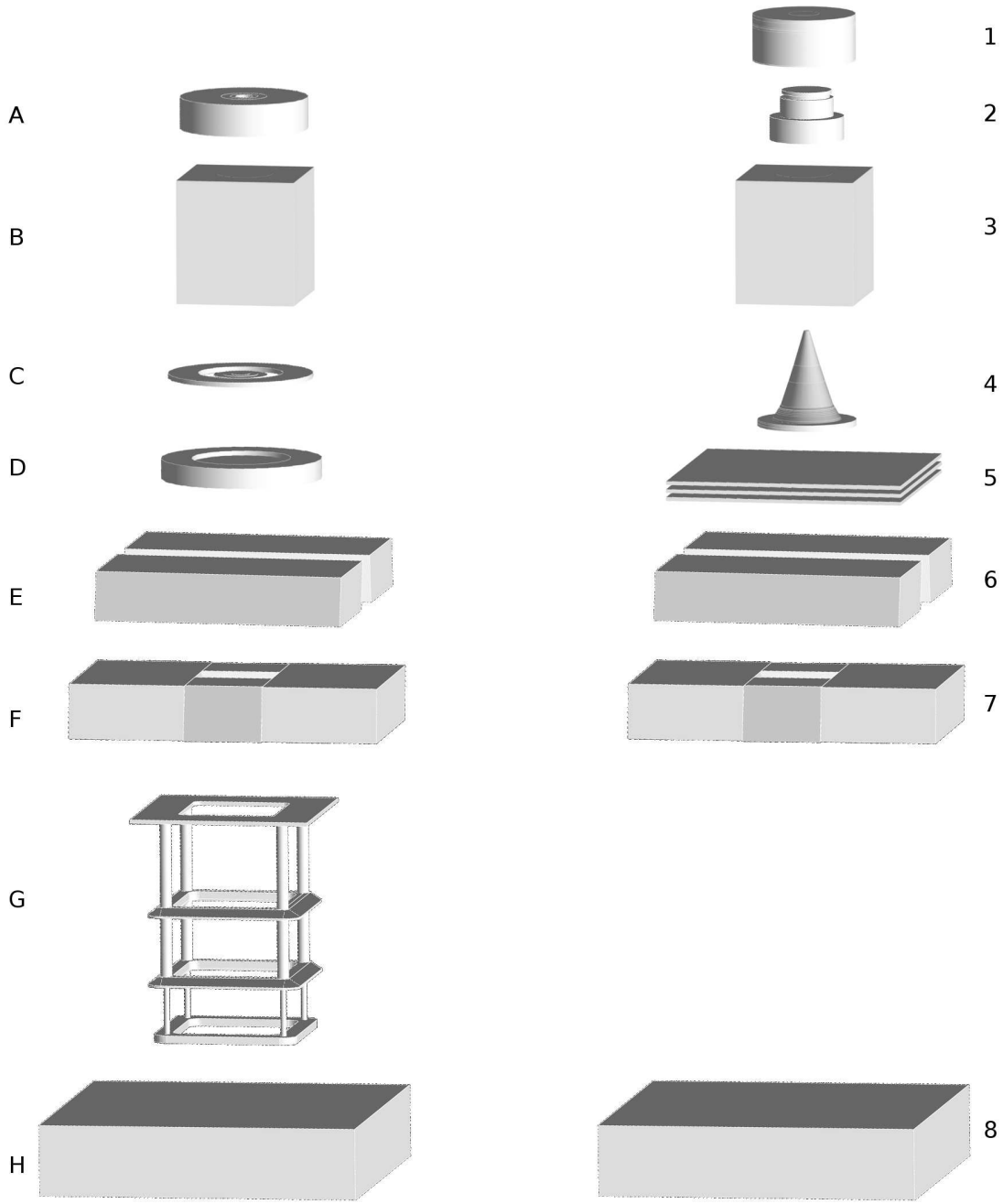

(a) Electron irradiation setup

(b) Photon irradiation setup

Figure 6.1 Setup of the irradiation system (beamdirection: top to bottom, exploded view, measures not to scale).
(a) Electron irradiation: primary foil (A) - primary collimator (B) - secondary foil (C) - electron dose chamber (D) - x-collimator (E) - multi leaf collimator (F) - electron applicator (G) - water phantom (H).
(b) Photon irradiation: target (1) - electron absorber (2) - primary collimator (3) - flattening filter (4) - photon dose chamber (5) - x-collimator (6) - multi leaf collimator (7) - water phantom (8).

leads to an enlarged penumbra and a less strictly defined irradiation area. The electron applicators allow the collimation of the electron beam close to the patient, but care has to be taken of the side leakage of electrons and photons. As more and more objects are inserted in the electron beam, the amount of secondary particles is increasing. These additional particles can deposit dose in healty tissue, which has to be avoided.

6.3 Photon Irradiation

The photon irradiation has to meet similar standards as well as the electron irradiation regarding homogeneity and flatness of the dose inside the irradiation area. As the acceleration unit is the same as for the electron irradiation, the photons have to be generated through Bremsstrahlung in a target and the remaining electrons have to be suppressed in the irradiation field. The beam is shaped by an energy-dependent flattening filter and collimated by the main x- and y-collimators. A schematic drawing of the complete photon irradiation configuration is shown in figure 6.1(b).
The photons are generated in a transmission target, which is placed in the primary eletron beam directly behind the exit window. The target is cooled by surrounding water, as a lot of the energy of the electrons is transferred to the material in a very small volume. The water cooling is not included in the simulation, as the water is not in the primary beam and the surrounding materials are strongly absorbing, so the water is not taking part in the beam shaping or photon generation.
Behind the target, an electron absorber is needed to restrain the remaining electrons from the patient, as the electrons would lead to an increased skin dose. The photons can easily pass through the absorber, and have to be shaped afterwards. As the distribution is not homogeneous and flat after the target, a flattening filter is placed in the beam. The energy-dependent flattening filter is used to modify the intensity and distribution of the photon irradiation.
Again, the flux of the photons is inspected by a photon dose chamber, which is different from the electron dose chamber due to the different interactions. The dose measured between the flattening filter and the collimation system is included in the feedback control of the electron acceleration.
The medical linear accelerator head has to provide multiple moving parts, as the setup has to be modified between different irradiation modes. Additionally, the flattening filters for the photon irradiation has to be exchanged for different applied energies.

6.4 Data Analysis

In the real setup, the only accessible measure of the irradiation is the applied dose. The simulation can rebuild the measurement and then yield additional information. The Monte-Carlo simulation results in a condensed history for each particle and all secondary particles.
The main measurement is performed with a water phantom which is placed at the position of the patient. Inside this phantom, the dose can be measured electronically as a function of depth and lateral displacement. Additionally, films can be placed anywhere in the setup, but films can only show the integrated dose distribution weighted with the

conversion curve which leads to difficult interpretation of the results.
In the simulation, the water phantom is also present and the deposited energy is accessible as a function of space. Despite the water phantom measurement, different other measurements even with films can be modelled, as the trajectories of each particle can be monitored.
Any geometrical object in the simulation can be used as a detector. This allows the observation of multiple measurement volumes within a single simulation. The information gained for all interactions points inside a registered object is stored during the simulation. When the Monte-Carlo simulation is finished, the stored information can be exported into histograms. The typical line scans (depth dose distribution and lateral dose profiles) and area plots (dose distribution in a slice) are realised as one- or two-dimensional histograms [42]. The spatial integration over reasonable volumes leads to smooth plots in reasonable computing time.
The advantage of the simulation is the availability of additional information like the number of particles, the spectral distribution of the particles or even the possibility to distinguish between the dose coming from electrons or photons. These quantities can be extracted from the stored information which is available in any registered volume.

7 Results

The following section presents results obtained with the Monte-Carlo tool Geant4 and some comparisons with measurements. The detailed geometrical dimensions have been determined in cooperation with the Siemens AG, Healthcare Sector. Many of the results are also part of the diploma thesis by Ina Münster and parts are published in [43]. As her diploma thesis was supervised by the author of this work, many aspects were observed in close collaboration.

7.1 Electron Irradiation

Clinical irradiation simulation is used for treatment planning and hence aims for the calculation of applied dose inside a treatment volume with a special interest in computation speed [44]. The dose calculation is based on lookup tables and probability functions [45]. In many cases, the Monte-Carlo simulation is starting from a basic model of the irradiation at the exit of the linear accelerator and is focussing on the dose distribution in medical samples.
The simulation presented in the following starts at the exit window of the energy selective bending magnet. In contrast to former publications, the simulation is focussing on the beam characteristics and not on the dose distribution in a medical phantom. The final collimation in the electron irradiation is done by the electron applicator. The simulations are performed for the 20*20 applicator, which limits the irradiated area to a quadratic field with 20 cm edge length.

7.1.1 Validation of the Simulation

A simulation can only be used for the evaluation of parameters, when the simulated data coinsides with real measurements. As the dose distribution inside a water phantom is accessable in the measurement, the simulation yields the same measurand. All incoming particles in the water phantom lead to deposited energy inside the volume. The deposited energy is converted into a dose by taking into account the deposition volume. The well defined depth dose distribution, which can be found in the literature (see figure 5.3), can be obtained in the central irradiation field. In figure 7.1 the dose distribution as a function of penetration depth in water is plotted.
The simulated data is compared to measurements, which were taken at a medical linear accelerator in a test cell. The agreement is within the expected range with respect to the spread between the measurements which is shown for the initial energy of 6 MeV. Additionally, the spectral distribution of the electrons in the measurement is not known exactly, which can lead to variations in the slope of the curve. But the depth dose maxima coincide very well between measurement and simulation.

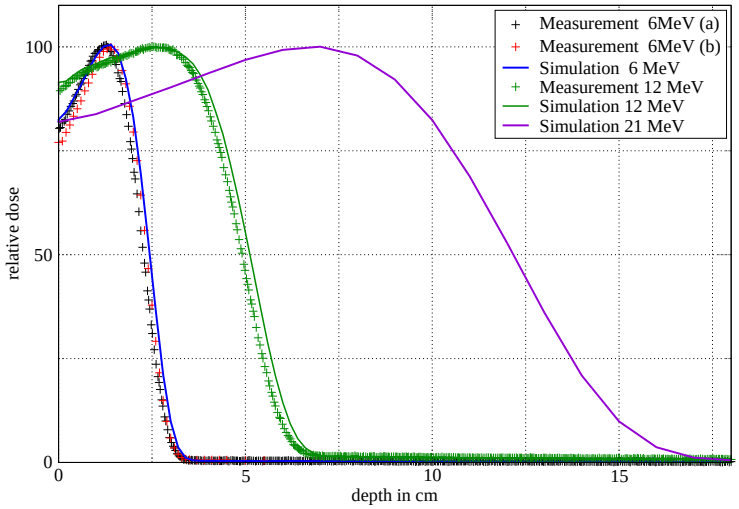

Figure 7.1 Depth dose distribution for different electron energies normalised to the dose maxima. Two measurements of the initial energy of 6 MeV (red and black crosses) are plotted to show the spread of different measurements. The simulation (blue line) is within the spread of the measurement in the relevant range of high dose. The agreement for the initial energy of 12 MeV is within the expected range, as the depth dose maxima coincide very well. There was no measurement taken for the 21 MeV as the medical linear accelerator used for the measurement was not capable of energies above 15 MeV.

The validation of the simulation can not only rely on the comparison of depth dose distributions. The measurement of lateral dose profiles inside the water phantom at different penetration depths is also needed. In figure 7.2, the dose in a slice in 2 cm penetration depth of the water phantom is shown. The dose is summed up over a slice thickness of 1 cm, i.e. between 2 cm and 3 cm. Lateral dose profiles are obtained from this slice by summing over the indicated areas. The summation is needed to reduce the statistical fluctuation without having to increase the number of simulated particles. The areas are selected to make use of the square area irradiated without taking the edges into the evaluation. This leads to comparable results as a line scan in the center of the area.
The simulation of such lateral dose profiles inside the water phantom is rather difficult as a very high number of initial electrons needs to be simulated to acquire sufficient dose deposition in the phantom[1]. The measurement data is taken with about $3 \cdot 10^9$ initial electrons for each of the measurement points. The number of electrons used for the simulation are 10^8 for all measurement points together. This explains the strong fluctuations of the simulated data with respect to the very smooth measurement data in figure 7.3.
The dose chamber in the measurement (PTW Dosimetry Diode E Type 60012, [47]) has a sensitive volume of $2.5 \cdot 10^{-3}\,\mathrm{mm}^3$ and is moved in steps of 0.5 mm. In the simulation, the applied dose is sampled with a binning of 0.5 mm to achieve the same precision as in the measurement and to allow sampling of the steep gradients. The volume for each sampling

[1] During the evaluation of the lateral dose profiles, a problem with the Monte-Carlo toolkit was discovered. The problem report [46] explains a possible work around, but the problem shows necessary improvement of the software.

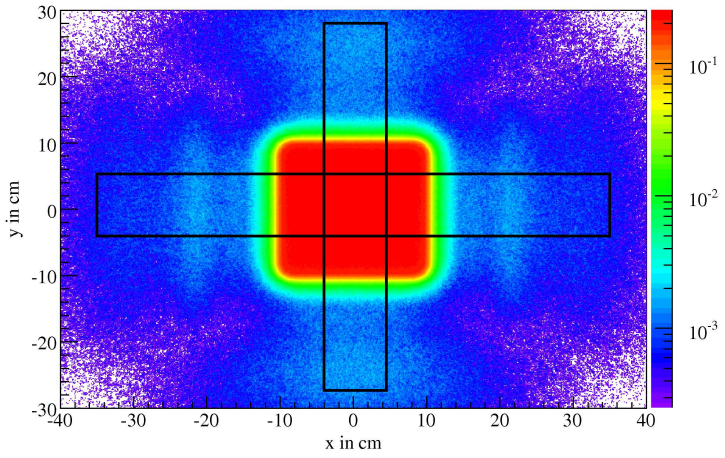

Figure 7.2 Dose distribution in a water phantom for electron irradiation with a primary mean energy of 12 MeV in a penetration depth between 2 cm and 3 cm. The main irradiation area is clearly visible in the centre, but also the deposited energy outside the illuminated area can be evaluated. The indicated areas are taken into account for extracting lateral dose profiles by summing up the deposited energy in one dimension.

point is elongated in the perpendicular direction to compensate for the low number of electrons in the simulation as indicated in figure 7.2.
As the energy of the initial electrons can be changed during irradiation, the validation has to be extended to more than just one energy. The depth dose profiles were shown in figure 7.1, but the lateral dose profiles inside the water phantom are also part of the validation. In figure 7.4, the measurement is compared to the simulation for an initial energy of 12 MeV. The agreement is again very good so the simulation can be used to investigate the influence of different parameters without constructing prototypes for each configuration.

7.1.2 Analysis of Parameters

The mechanical setup for each applied energy is very similar: only the primary scattering foil and the collimation window of the main collimators are changed with energy. This is done to balance the quality of the flatness of the applied dose, the shape of the penumbra and the scattered radiation which leads to dose deposition outside the irradiation area.

Initial Energy

The initial energies of the electrons used in medical irradiation are in the range between 6 MeV and 21 MeV. As the spectral information is not easily accessible in the experiment, the tuning to the energy is done indirectly: the depth dose distribution is measured, and the energy is tuned to a value to adjust the depth dose maximum to a certain value. These energy-dependent depth dose maxima are taken from literature. The tuning to the exact energy is therefore depending on the specific setup and can vary for each assembly. The aim is to adjust the depth dose distribution for each irradiation unit and allow the

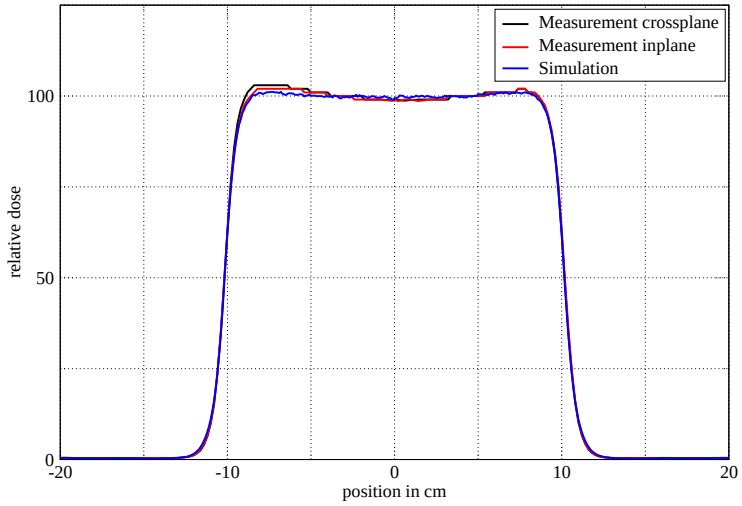

Figure 7.3 Lateral dose profiles for electron irradiation with a primary energy of 6 MeV normalised to the means of the plateau level. The measurement is taken at a penetration depth of 13.6 mm in x- and y-direction, and in the simulation, the dose contribution between 1 cm and 2 cm is summed up. The plateau level is not part of the comparison as the exact beam parameters are not known, but the focus is on the strong slope of the edge of the irradiation area.

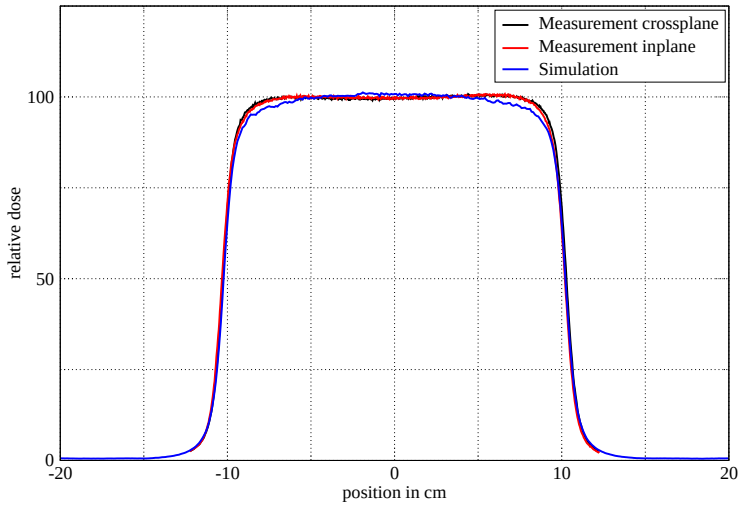

Figure 7.4 Lateral dose profiles for electron irradiation with a primary energy of 12 MeV normalised to the means of the plateau level. The measurement is taken at a penetration depth of 20.8 mm in x- and y-direction, and in the simulation, the dose contribution between 2 cm and 3 cm is summed up. The plateau level is not part of the comparison as the exact beam parameters are not known, but the strong slope is simulated very well.

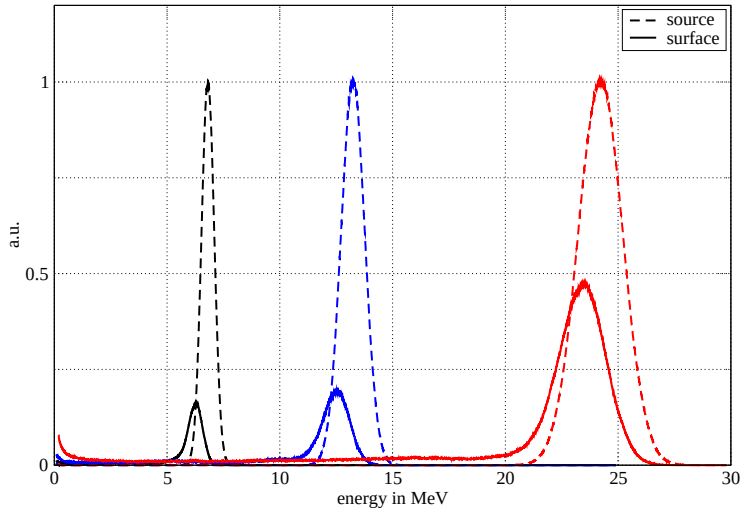

Figure 7.5 The spectral distribution of the electrons at the exit window (dotted line) and at the surface of the water phantom (solid line). The energy at the exit window is higher than the nominal energy in all three cases (6 MeV black, 12 MeV blue and 21 MeV red). The shift and broadening of the energy distribution is due to the scattering in the air and the scattering foils, which are present between the exit window and the water surface. The scattering is also the reason for the decrease of the area below the graphs.

use of the same nominal energy with different units. The simulation offers the possibility to study the spectral distribution at selected positions within the simulation setup.
In figure 7.5, the spectral distribution of the electrons at the exit window for different energies is plotted in comparison to the spectral distributions at the surface of the water phantom. The distribution is broadened and shifted to lower energies due to the scattering processes in the scattering foils and due to the air which is present between the exit window and the water phantom. The spectrum at the surface penetrates into the water phantom and deposits the dose inside the phantom. The depth dose distributions of the different electron beams are shown in figure 7.1.

Dose Distribution

The dose distribution is a function of the depth, but also depends on the lateral position. The irradiation is limited to an illuminated area and scattering processes lead to dose deposition outside this area. In the left part of figure 7.6, the dose distribution in a water depth of 2 cm is shown for a simulation case which is very close to the measurement. The main illumination can clearly be seen, and the dose deposition outside the irradiation area is a lot smaller. For a better comparison, profiles through the main irradiation area are taken as labelled in figure 7.2. The dose distribution is very homogeneous inside the indicated areas, which allows to take an average over a region in the y-direction to gain a smoother profile in the x-direction without increasing the computing time.
The difference between the left and the right part of figure 7.6 is the collimation which is performed. In the measurement, the electron beam is first collimated in the y-direction

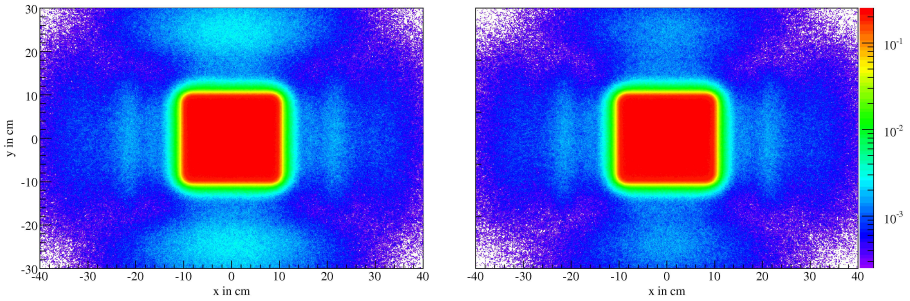

Figure 7.6 Dose distribution in a water depth of 2 cm. The left image shows the simulation which is calculated for the given setup and which is very close to the measurement. In the right image, the multi leaf collimator is used to additionally collimate the y-direction. The dose reduction outside the irradiation area is clearly visible above and below the irradiation area.

and subsequently in the x-direction. This leads to a longer free travelling distance between the collimation and the detection in the y-direction. Hence, more scattering can occur, which leads to dose contribution outside the main irradiation area. The collimation of the y-direction can be supported by the multi leaf collimator which is designed to collimate the x-direction. This additional collimation leads to a reduction of the dose outside the irradiation area.
The x- and y-dimensions of the beam source are different in the simulation as they are also different in the experiment. In the x-direction, the size of the beam spot is modelled with a Gaussian profile. In the y-direction the same profile is used, but is extended due to the energy spread which can pass through the bending magnet. The difference between the two main directions of the electron source is visible in the measurement as plotted in figure 7.3, where the x-direction (crossplane) shows less elevation on the edge of the irradiation field.
The energy-dependent distribution of the photons in the source beam spot leads to different spectral distributions of the electrons in the beam with respect to the y-direction. This effect can be observed in the figure 7.7: the collimation is done identically, but the y-direction shows a tilting in the dose profile. The tilting is due to the different spectral distribution and hence the different depth dose profiles for different y-positions in the electron beam.
In figure 7.8, the dose distribution is shown as a function of the lateral position and the depth. The water phantom surface is the clear line at the bottom and the electron irradiation is impinging from beneath. The three different images show the dose distribution for three different energies, increasing from left to right. The increasing penetration depth with increasing energy is superimposed with the divergence of the electron beam. For different water depths, x-profiles are plotted in figure 7.9 for the 12 MeV electron beam to show the buildup effect and the divergence of the dose distribution. The maximum levels in the centre of the x-profiles follow the depth dose profile from figure 7.1.

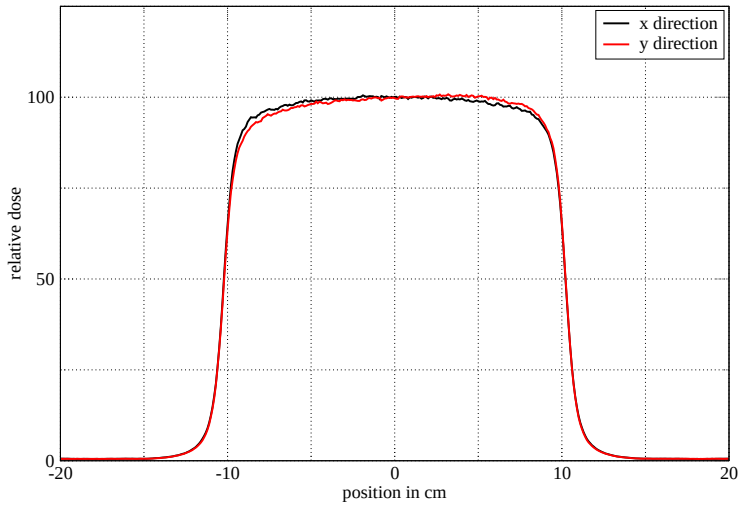

Figure 7.7 Dose profiles in a water depth of 2 cm. The y-direction is tilted with respect to the x-direction as the spectral distribution varies as a function of the y-postion due to the spread in the energy selection of the bending magnet.

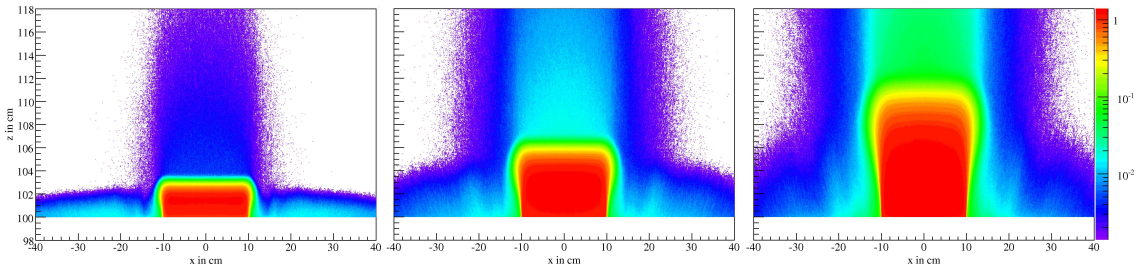

Figure 7.8 Dose distributions in a water phantom. The three different energies (left: 6 MeV, middle: 12 MeV and right: 21 MeV) have increasing penetration depths and show the divergence of the electron beam which is impinging from the bottom. The dose distribution due to generated photons is clearly visible: all impinging electrons are stopped in the red high dose area (main illumination area), but photons generated by Bremsstrahlung penetrate deeper in the material. The photon contribution of the applied dose is increasing with energy. Additionally, the dose outside the main irradiation area (by electrons and photons) is increasing with energy as the collimation system is not capable of stopping all particles when the energy is increased.

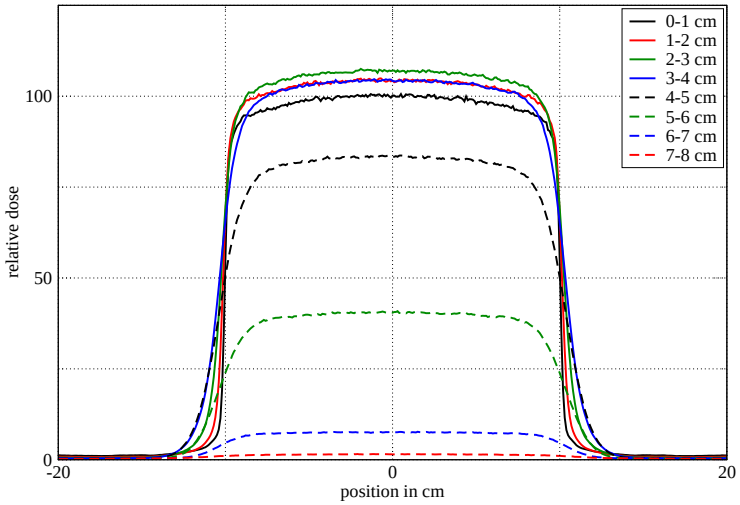

Figure 7.9 Dose profiles in a water phantom for a 12 MeV electron beam for different water depths. The profiles show the buildup effect as the main level is first increasing with increasing depth, but then decreasing. Additionally, the broadening of the profile due to divergence and scattering is clearly visible. The dose profiles are scaled relative to the surface dose in the center of the beam.

Spectral Analysis

Another advantage of the simulation is the possibility to gain information about the spectral distribution of the electron beam in any position. The change in the spectral distribution of the electrons can be observed as a function of penetration depth in water. In figure 7.10, the spectrum of the electrons is plotted for increasing water depth. The spectrum is shifted to lower energies and the main energy is decreased. As the area beneath the spectral curve is a measure for the amount of electrons, the integral over the curve is decreasing with increasing penetration depth. The electron beam has 12 MeV initial energy and the dose for each depth follows the depth dose distribution as in figure 7.1. The strong increase for low energies is due to the secondary electrons which are generated by interaction in the water.

Side Leakage

In the electron irradiation, the collimation is achieved by the main collimators and additionally with the electron applicator to collimate the electron beam close to the patient. As the electron applicator is used only in the electron irradiation and has to be removed for photon irradiation, the weight of the applicator needs to be limited to a reasonable amount because it is handled by clinical personnel. The collimation of high energetic electrons is done by absorption and scattering in the scraper of the applicator. But this scattering leads to secondary electrons and photons which are not wanted inside the main irradiation area.
However, the radiation which leaves the applicator on the side is part of ongoing research interest as this radiation can lead to dose application in the patient outside the irradiation

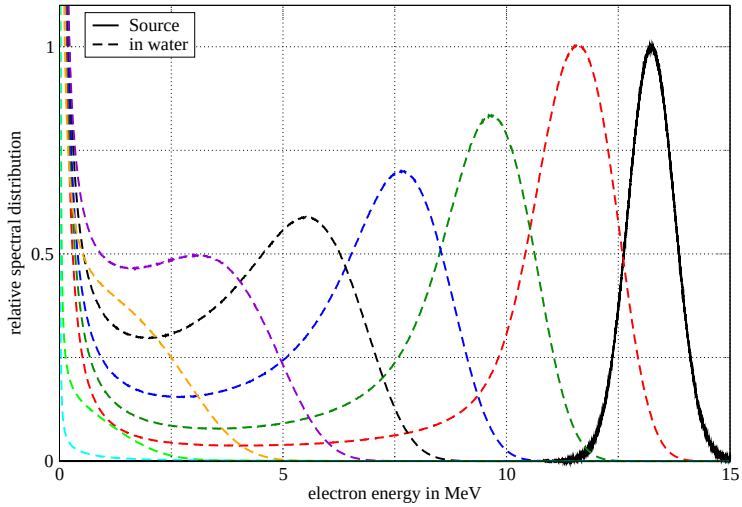

Figure 7.10 Spectral distribution of the electrons as a function of penetration depth. The black solid line is the normalised inital spectrum from the source. The dashed lines show the spectrum in the water phantom as a function of depth in steps of 1 cm (1 cm [red], 2 cm [green] et seq.). The energy is shifted to lower energies with increasing depth. The height of the spectral distributions in water is scaled to normalise the peak maximum of the spectrum for a depth of 1 cm (red line). The strong increase at very low energies is due to secondary electrons generated during interactions. The plateau between the main peak and the low energy increase is due to electrons loosing parts of their energy by scattering and afterwards leaving the volume.

area. The side leakage can be observed around the electron applicator, and the dose may not exceed a certain value at any point on the observation area. The observation is usually done with a film or with a multi-array dosimeter. In the simulation, all particles which pass through a surface around the electron applicator are taken into account to measure the side leakage dose.
In figure 7.11, the dose distribution around the electron applicator is shown. The four parts correspond to the four sides of the applicator. The source is at the bottom, so the electrons are directed upwards. To investigate the effect of the electrons and the Bremsstrahlung photons to the dose, the number of particles which pass through the measurement surface is plotted in figure 7.13. The contribution of the photons to the dose has only minor influence, as the main dose component is due to the electrons.
The number of electrons can be reduced significantly when the collimation is optimised. The illumination area is collimated in the y-direction by the main y-jaws and in the x-direction by the multi leaf collimator (MLC). The additional collimation by the applicator is applied between the main collimation and the patient plane. The differences between the x- and y-direction are due to two effects: firstly, the primary electron distribution at the exit window of the acceleration unit behind the bending magnet has a large diameter in the y-direction and secondly, the main y-collimation is performed closer to the source than the main x-collimation. This leads to a longer travelling distance of the electrons between the collimation plane and the applicator and hence more scattering in the surrounding air.

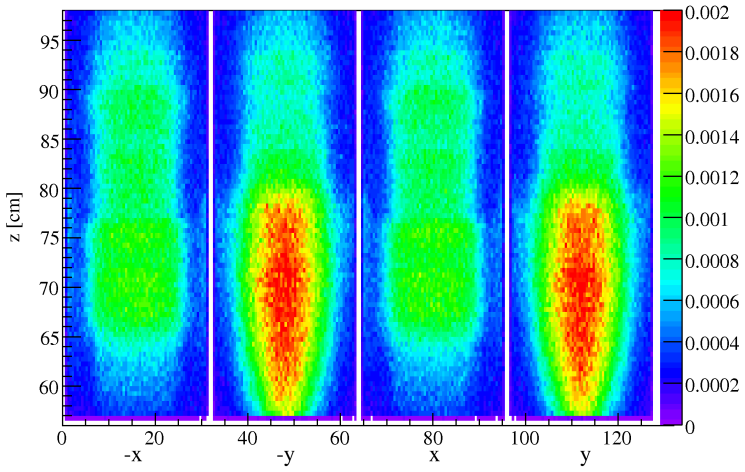

Figure 7.11 Side leakage dose distribution around the electron applicator. The electrons are impinging from the bottom with an initial energy of 12 MeV. The four columns represent the surface of a measurement box around the applicator. As the y-direction is collimated at a position closer to the source, i.e. further away from the detection plane, it shows a lot more leakage dose. This originates from more scattering with air on the way from the main collimation to the applicator.

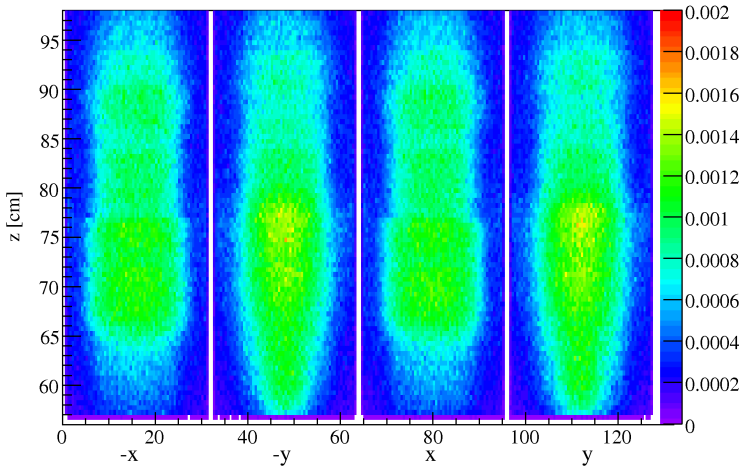

Figure 7.12 Side leakage dose distribution with additional y-collimation with the multi leaf collimator. The electrons are impinging from the bottom with an initial energy of 12 MeV. Geometry and color scale is the same as in figure 7.11. Obviously, the dose in the y-direction is reduced significantly.

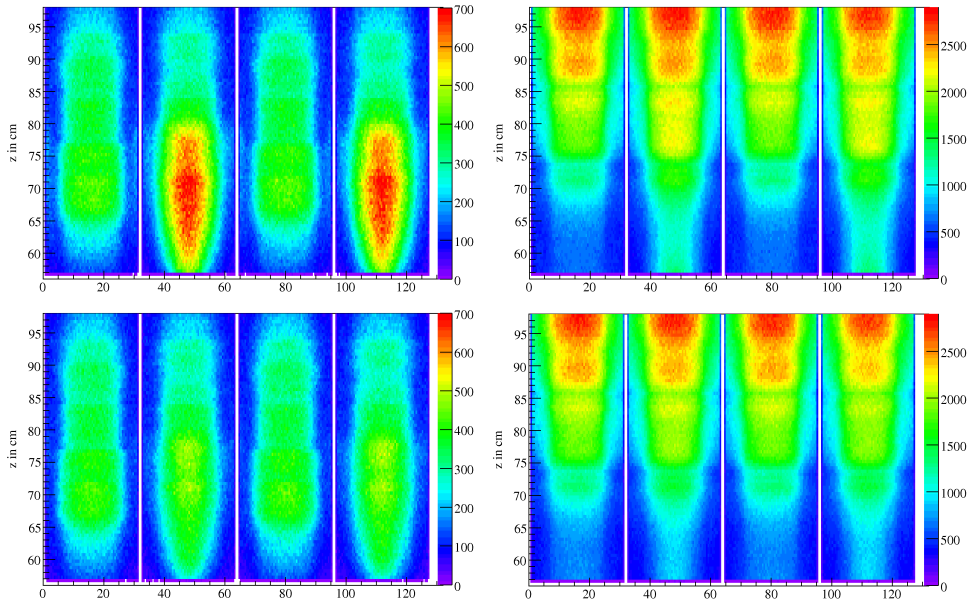

Figure 7.13 Number of particles passing through the measurement surface in the same geometry as in figure 7.11 (left: electrons, right: photons). In the top row, the y-collimation is done only by the y-collimator, whereas in the bottom row, the y-collimation is additionally performed by the multi leaf collimator (MLC). The dose distribution in figure 7.11 is dominated by the electrons. The reduction of the number of electrons in the side leakage with the MLC is prominent. The photon leakage is only slightly reduced.

The source cannot be optimised easily, but the main y-collimation can be supported by the MLC. The MLC has thin slits, which have a projected thickness of 5 mm in the iso surface. The collimation of the x-direction can be done in steps of this projected thickness only, but this is sufficient as the applicators are manufactured in discrete steps. Closing the leaves which are outside the main electron field leads to an almost symmetrical collimation of the x- and y-direction at the z-position of the MLC. The improvement of the side leakage can be seen in figure 7.12. The effect is mainly based on the electron leakage, which is shown by comparing the two rows in figure 7.13.

7.2 Photon Irradiation

In contrast to electron irradiation, photon irradiation does not need a collimation close to the patient, as the photon beam is not broadening due to scattering in the air as much as the electron beam. Concurrently, dose deposition is not as localised to the surface as in the electron case. The depth dose maximum is directly at the surface for photon energies below 300 kV and rises to 1.5 cm for 6 MV and 2.5 cm for 10 MV [48]. The energies are labelled in "Mega Volts" and not in 'Mega Electron Volts' as in the electron irradiation, because the whole photon spectrum produced by an electron beam of the named energy is considered. In figure 7.14, the simulated depth dose distribution for photons is shown which show a good agreement of the depth dose maxima with the data from literature. The buildup region is less prominent than in the electron irradiation, and the falling slope

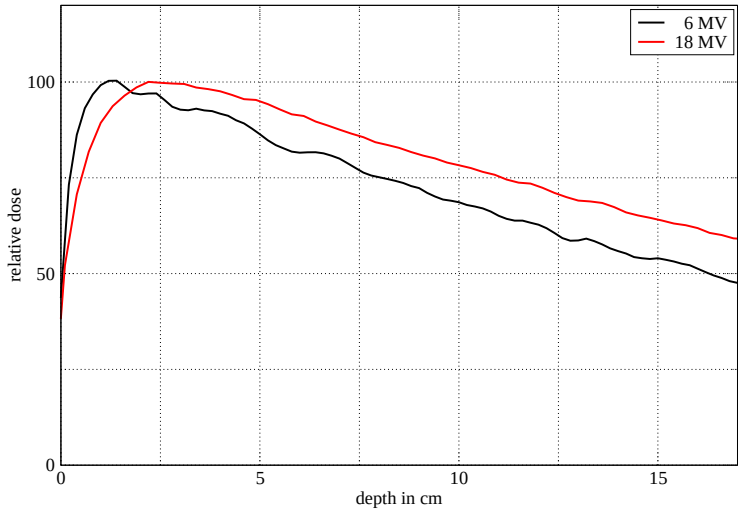

Figure 7.14 Depth dose distribution for different photon energies. In contrast to the electron depth dose in figure 7.1, the variation of the depth dose distributions in the photon case is only very little.

is decreasing slower.
The penetration depth is a lot larger than for the electrons, and the variation due to different initial energies is less prominent. An important issue for the photon irradiation is the reduction of the surface dose, as the irradiation penetrates deep into the volume, and therefore photons are used to treat inner tumours. An important part of the surface dose reduction is to avoid electrons from the initial beam to hit the surface. An electron absorber is inserted directly behind the target. The ratio of electrons and photons in the irradiation beam is below 2% behind the electron absorber. Additionally, the fraction of low-energetic photons should be kept small. This is important in the penumbra region, where parts of the main beam are collimated, but scattered radiation may pass through. In figure 7.15, the dose distribution in the water phantom is plotted in a penetration depth between 2 cm and 3 cm. The main irradiation photon field is clearly visible. But the scattered radiation (photons and electrons) deposit energy all over the water phantom.
The penetration depth is only varying a little with the initial energy, therefore only the dose distribution for 15 MV initial energy is plotted in figure 7.16 as a function of lateral position and penetration depth. The divergence of the beam can be observed.
Again, the simulation offers the possibility to acquire information on the spectral distribution of the beam. The initial electron beam hitting the target is defined by the accelerator. The Bremsstrahlung spectrum which is emitted from the target is shown in figure 7.17 in comparison to the primary electron spectrum. As the definition of the initial photon energy is difficult, the depth dose distribution in water is measured: the depth dose maximum are defined for photon beams the same way as for electron beams to be able to use different linear accelerator assemblies with the same nominal energies.
The spectrum at different penetration depth in the water phantom is plotted in figure 7.18. As with electrons, the integral of the spectrum, which is a measure of the number of pho-

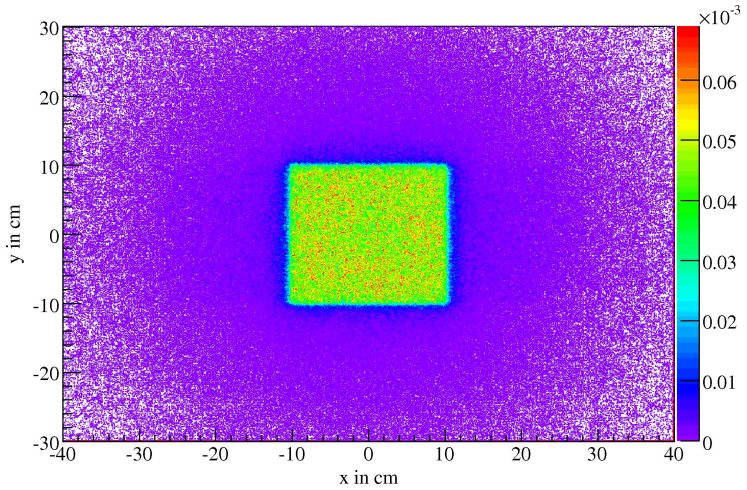

Figure 7.15 Dose distribution for an incoming 18 MV photon beam. The main irradiation area can be clearly spotted, but scattered irradiation deposits dose even far away from the main irradiation area.

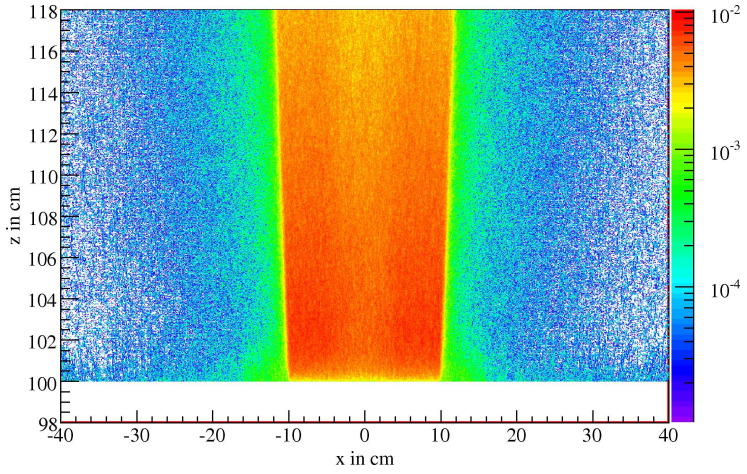

Figure 7.16 Dose distribution for an incoming 15 MV photon beam as a function of penetration depth and lateral dimension. The field size is $20 \times 20\,\mathrm{cm}^2$. The water surface can be clearly spotted at $z = 100\,\mathrm{cm}$.

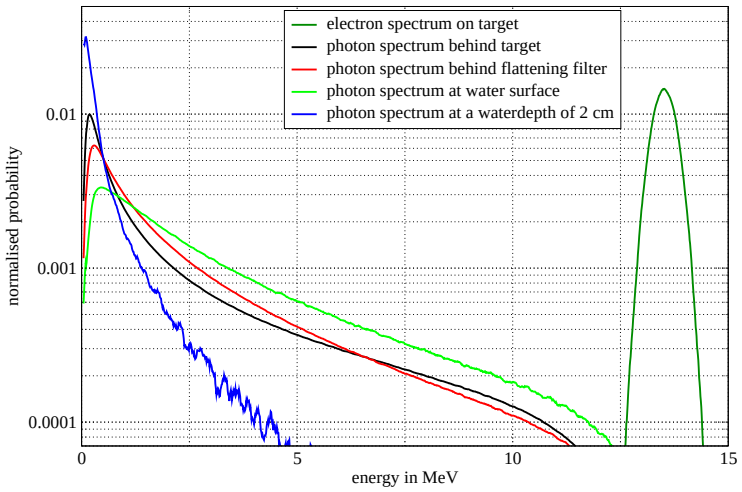

Figure 7.17 Spectral distribution of the primary electron at the exit window (green line) and of the photons which are emitted by the target (black line). The spectra are normalised to one. The initial electron energy is 13 MeV which corresponds to the 15 MV photon mode. The photon spectrum behind the flattening filter is marked in red. The flattening filter and the surrounding air result in a reduction of the number of low energy photons, which leads to the green line which corresponds to the photon spectrum impinging on the water surface. In the water, secondary photons are generated by Bremsstrahlung which leads to an increasing number of low energy photons. An example of the spectral distribution of photon in the water phantom is plotted in blue.

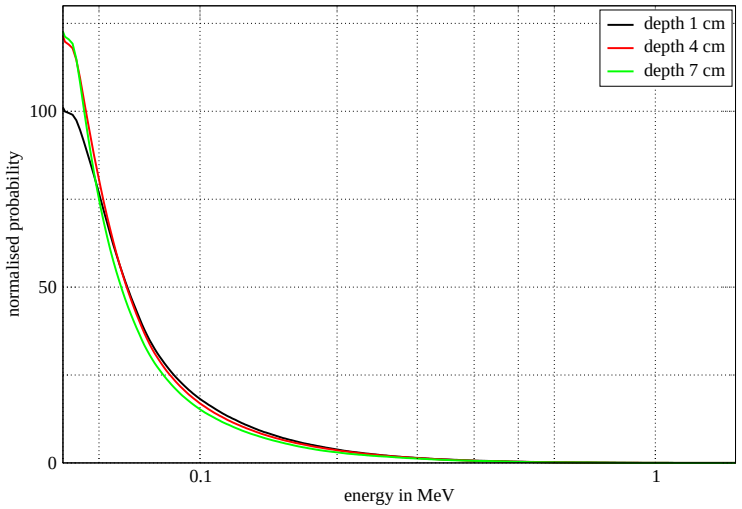

Figure 7.18 Spectral distribution of the photons in different penetration depths. The energy axis is in logarithmic scale. The spectral distribution is hardly changing, only very few X-ray photons are scattered to lower energies. The probability is normalised to the low-energetic end of the black line (depth 1 cm) and the lines for other depths are scaled due to the areas below.

tons, follows the depth dose distribution in figure 7.14. In contrast to the electron case, the spectrum is not changing significantly.
For photon irradiation, the multi leaf collimator can be used to form the irradiation area. It is possible to limit the beam to the shape of the tumour and so protect surrounding tissue from being irradiated. This is important due to the high penetration of photons in the human tissue.

8 Summary and Discussion of Part II

The simulation of the medical irradiation module with the Monte-Carlo tool Geant4 offers the possibility to follow each individual particle on its passage through matter. This direct access to the trajectory of the particles is a powerful tool to gain more information on the system. In contrast to the clinical Monte-Carlo simulation, the focus of the evaluation was not set to the applied dose to a patient, but to the observation of the characteristics of the irradiation head.

The photon irradiation mode simulation was build up based on the technical details of the manufactured parts in the beam line. The simulation starts with the impinging electrons and the photon generation in the target is modelled. The flattening filter and the beam collimation are part of the simulation as well. The depth dose curves show good agreement with the data from literature as shown in figure 7.14. The distributions of the impinging particles on the water surface are a kind of information which is not accessible in the measurement. The possibility to distinguish between electron and photon contribution to the dose can lead to an improved knowledge on the initial particle distribution in the measurement and show ways to improve the photon distribution.
The dose distribution in figure 7.16 shows the need for multifield irradiation in the case of photon irradiation. As the dose deposition is very homogeneous with increasing depth, the dose can be increased in the target volume, i.e. the tumour, by irradiating from different directions. This is part of the dose planning systems which are used in clinical environments. But these dose planning systems need to have a detailed knowledge on the particle beam which is coming out of the accelerator. The simulation allows to study not only the dose distribution but also the spectral changes when the beam path is modified either by collimation or inserting scattering parts. The spectral study can improve the model of the accelerator head used in the dose planning systems.

The electron simulation contains a detailed model of the experimental setup. This allows the validation of the simulation by direct comparison of the simulation and the measurement results. The agreement between the simulated and measured dose distributions is very good as pointed out in figures 7.1 and 7.3. This encourages the evaluation of possible improvements of the electron irradiation. As shown in figure 7.6 the dose outside the irradiation area can be reduced by applying the multi leaf collimator (MLC). The additional collimation of the y-direction reduces the dose without disturbing the quality of the beam inside the irradiation area.
The reduction of the dose outside the main illumination area is also clearly visible in the dose contribution which leaves the electron applicator at the side. Any particle leaving the applicator on the side is on the one hand lost for the main irradiation purpose and can on the other hand deposit its energy in sensitive healthy regions of the patient. The closing of the MLC leads to less particles leaving the electron applicator without affecting

the flatness of symmetry of the main irradiation beam.
Information which is hardly available in the measurement is the spectral distribution of the particles in the beam. The knowledge of the spectral components and particle sorts at certain positions can be used to improve the collimation efficiency, as electrons can be stopped by light materials whereas photons are only attenuated. The electrons are additionally collimated by the electron applicator, but in the photon mode no applicator is needed. This requires the mounting and dismounting of the electron applicator for each irradiation procedure. The weight of the electron applicator is therefore competing with the collimation efficiency. In the diploma thesis of Ina Münster, the weight reduction of the electron applicator is part of the topic.

The simulation is built up to a stage where effective studies on collimation and beam shaping parts can be performed. Additional information gained with the simulation can be used to optimise the setup and develop future medical irradiation systems.

Summary

This thesis aims for an improved understanding of medical irradiation. Two major parts are investigated: the beam shaping components of a medical linear accelerator, i.e. the source of the radiation, and the signal generation inside semiconductor sensors, i.e. the detection of the radiation.

The direct measurement of the spatial and spectral particle distribution in the irradiation beam is not possible with state of the art detectors due to the high particle flux. The development of new advanced detectors is the goal of the first part of this thesis. The focus is set on the signal generation inside the sensor volume of a semiconductor detector. Incoming particles interact with the sensor material and generate clouds of electron hole pairs. These pairs get separated by an applied bias voltage. The motion of the charge clouds is simulated with a finite element programme taking into account the drift and diffusion.
Mirror charges are induced on the electrodes which move due to the motion of the charge cloud. The motion of the induced mirror charges leads to the signal that is detected. The transient calculation of the signals is based on Ramo's theorem. The efficient adjoint formulation of the induction solution is adjusted to doped materials, as for example the electric bias field and hence the motion of the charge cloud is changing with the doping level. The effect of the doping of the material on the signal shape is shown together with influences of different voltages and pixel geometries.
Smaller pixels and higher bias voltages can lead to shorter signals which is preferable for high flux measurements. Possible count rate improvements are limited by electric break through, high dark current across the sensor layer and charge sharing. Another option to shorten the signals is the use of steering grid electrodes which modify the electric and the weighting field. This results in shorter signals and thus in a higher possible rate.

The detailed Monte-Carlo simulation of the irradiation head of the medical linear accelerator is constructed for the irradiation with electrons and photons in the second part of this thesis. The simulation is validated by comparison with water phantom measurements. Available information from the measurements is limited to the depth dose deposition and dose profiles in selected water depths. The simulation allows the evaluation of dose depositions and spectral particle distributions at various locations. This will be used to optimise scattering foils and collimation geometries.
In the electron irradiation mode, a collimation close to the patient is performed by an electron applicator. The leakage radiation at the outside of the applicator needs to remain

below certain legal requirements. A possible reduction of the side leakage is evaluated by optimising the collimation of the beam. This can be achieved with the collimation system which is already part of the irradiation head and no additional components are required. Additionally, new beam shaping components can be designed and tested before prototyping. The influence of fabrication tolerances can also be evaluated.

Together, both parts of this thesis can help to improve the tumour treatment as cancerous diseases affect a growing number of human beings. Medical irradiation with MeV-electrons and X-ray photons is the part of the clinical tumour treatment which is evaluated in this work. Both types of irradiation deposit energy inside the tumour cells and lead to lethal damages of the DNA inside the cells' nucleus. For a successful treatment it is crucial to force all tumour cells into apoptosis while keeping healthy surrounding cells alive. This requires the exact planning of the dose deposition inside the volume, which can only be based on a detailed knowledge of the irradiation beam.

Zusammenfassung

Diese Arbeit zielt auf ein besseres Verständnis der medizinischen Bestrahlung ab. Dafür werden zwei Themenbereiche untersucht: die strahlformenden Elemente des medizinischen Linearbeschleunigerkopfes, das heißt die Quelle der Strahlung, und die Signalerzeugung in einem Halbleitersensor, das bedeutet die Detektion der Strahlung.

Die direkte Messung der räumlichen und spektralen Teilchenverteilung im Bestrahlungsfeld ist mit aktuell verfügbaren Detektoren wegen des sehr hohen Teilchenflusses leider nicht möglich. Die Weiterentwicklung von Detektoren ist Thema des ersten Teils der Arbeit. Der Fokus liegt dabei auf der Erzeugung von Signalen im Sensorvolumen eines Halbleiterdetektors. Einfallende Teilchen wechselwirken mit dem Sensormaterial und erzeugen Elektron-Loch-Paare am Wechselwirkungsort. Diese Ladungspaare werden durch ein anliegendes elektrisches Potential getrennt und bewegen sich auf die entsprechenden Elektroden zu. Die Bewegung der Ladungswolken wird in einem Finite-Elemente-Programm unter Berücksichtigung von Drift und Diffusion berechnet.
Auf den Elektroden werden Spiegelladungen influenziert, die sich entsprechend der Bewegung der Ladungswolke im Sensorvolumen verschieben. Die Bewegung der influenzierten Spiegelladungen führt zu einem Signal, das mit einer Ausleseelektronik detektiert wird. Die zeitabhängige Berechnung der Signale basiert auf dem Theorem von Ramo. Die effiziente adjungierte Formulierung der Influenzierung wird für die Anwendung in dotierten Materialen angepasst, da sich durch die Dotierung das elektrische Feld im Sensor und dadurch die Bewegung der Ladungswolke verändert. Der Einfluss der Dotierung auf die Signalform wird zusammen mit weiteren Einflüssen wie verschiedenen Verarmungsspannungen und Pixelgeometrien gezeigt.
Kleine Pixel und hohe Verarmungsspannungen führen zu kurzen Signalen, die für eine Messung mit hoher Rate notwendig sind. Die möglichen Verbesserungen der Messrate ist jedoch durch elektrische Überschläge, hohe Dunkelströme durch das Sensormaterial und Ladungsverteilung auf mehrere Pixel (charge sharing) begrenzt. Eine weitere Möglichkeit die Signale zu verkürzen, ist die Verwendung von Steering-Grid-Elektroden, mit denen das elektrische Feld und das Wichtungspotential beeinflusst werden können. Dies führt zu kürzeren Signalen und folglich zu der Erreichbarkeit höherer Messraten.

Für die Elektronen- und Photonenbestrahlung wird im zweiten Teil der Arbeit eine detailierte Monte-Carlo Simulation des Bestrahlungskopfes eines medizinischen Linearbeschleunigers aufgebaut. Die Validierung der Simulation wird durch den Vergleich mit Messungen am Wasserphantom durchgeführt. Die Ergebnisse der Messung sind allerdings auf

die Tiefendosisverteilung und Dosisprofile in verschiedenen Wassertiefen beschränkt. Bei der Auswertung der Simulation kann die räumliche und spektrale Teilchenverteilung an beliebigen Orten im Simulationsvolumen bestimmt werden. Dies ermöglicht die Optimierung von Streufolien und Kollimatorgeometrien.
Im Elektronenmodus wird die letzte Kollimierung erst kurz vor der Patientenebene mit einem Elektronenapplikator durchgeführt. Die Leckstrahlung, die den Applikator seitlich verlässt, muss gesetzlichen Bestimmungen entsprechen. Eine Variante zur Reduktion der Leckstrahlung wird mit Hilfe der im Bestrahlungskopf vorhandenen Kollimatorkomponenten vorgestellt. In diesem Fall sind keine zusätzlichen Komponenten erforderlich, aber neue strahlformende Elemente können entwickelt und getestet werden, ohne Prototypen für das reale Experiment herstellen zu müssen. Es kann auch der Einfluss von Herstellungstoleranzen untersucht werden.

Zusammen können die beiden Teile der Arbeit helfen, die Tumorbehandlung zu verbessern, was immer wichtiger wird, da die diagnostizierten Krebsneuerkrankungen stetig steigen. Medizinische Bestrahlung mit MeV-Elektronen und Röntgenphotonen ist der Teil der klinischen Tumorbehandlung, welcher in dieser Arbeit behandelt wird. Beide Strahlungsarten deponieren Energie in den Tumorzellen, was zu letalen Schäden an der DNA führt. Für die erfolgreiche Behandlung ist es notwendig, alle Tumorzellen in die Apoptose zu überführen und dabei die umgebenden gesunden Zellen zu schützen. Dies verlangt die genaue Planung der deponierten Dosis im bestrahlten Volumen, was nur auf der detailierten Kenntnis des Teilchenstrahls beruhen kann.

Bibliography

[1] X. Llopart, M. Campbell, R. Dinapoli, D. San Segundo, and E. Pernigotti, "Medipix2: A 64-k pixel readout chip with 55-μm square elements working in single photon counting mode," *IEEE Trans. Nucl. Sci.*, vol. 49, no. 5, pp. 2279–2283, 2002.

[2] K.-F. Pfeiffer, *Evaluation of the Medipix Detectors for Medical X-Ray Imaging, with Special Consideration of Mammography.* PhD thesis, Universität Erlangen-Nürnberg, Dec. 2004.

[3] J. Durst, *Modellierung und Simulation physikalischer Eigenschaften photonenzählender Röntgenpixeldetektoren für die Bildgebung.* PhD thesis, Unversität Erlangen-Nürnberg, July 2008.

[4] R. Ballabriga, M. Campbell, E. Heijne, X. Llopart, and L. Tlustos, "The Medipix3 Prototype, a Pixel Readout Chip Working in Single Photon Counting Mode With Improved Spectrometric Performance," *IEEE Trans. Nucl. Sci.*, vol. 54, pp. 1824–1829, Oct. 2007.

[5] S. Sze, *Semiconductor Devices - Physics and Technology.* John Wiley & Sons, Inc., 2 ed., 2002.

[6] A. Zumbiehl, M. Hage-Ali, P. Fougeres, J. Koebel, R. Regal, and P. Siffert, "Electric field distribution in CdTe and $Cd_{1-x}Zn_xTe$ nuclear detectors," *Journal of Crystal Growth*, vol. 197, pp. 650–654, 1999.

[7] A. Cola, I. Farella, N. Auricchio, and E. Caroli, "Investigation of the electric field distribution in x-ray detectors by Pockels effect," *Journal of Optics A*, vol. 8, pp. 467–472, 2006.

[8] S. Ramo, "Currents induced by electron motion," *Proceedings of the I.R.E.*, vol. 27, pp. 584–585, 1939.

[9] W. Shockley, "Currents to Conductors Induced by a Moving Point Charge," *Journal of Applied Physics*, vol. 9, pp. 635–636, 1938.

[10] C. Canali, M. Martini, and G. Ottaviani, "Transport Properties of CdTe," *Phys. Rev. B*, vol. 4/2, pp. 422–431, 1971.

[11] A. Korn, *Spektrale und bildgebende Eigenschaften photonenzählender Röntgendetektoren am Beispiel des Medipix-Detektors.* PhD thesis, Universität Erlangen-Nürnberg, May 2007.

[12] B. Kreisler, G. Anton, J. Durst, and T. Michel, "Charge Carrier Motion in Semiconductors," in *Proceedings of the COMSOL Users Conference Frankfurt, pp. 64-66*, 2006.

[13] V. Radeka, "Low-Noise Techniques in Detectors," *Annual Review of Nuclear and Particle Science*, vol. 38, pp. 217–277, Dec. 1988.

[14] B. Kreisler, "Influenzierte Signale in pixelierten Halbleiter-Röntgen-Detektoren," Master's thesis, Universität Erlangen-Nürnberg, May 2006.

[15] T. H. Prettyman, "Method for mapping charge pulses in semiconductor radiation detectors," *Nucl. Instr. and Meth. A*, vol. 422, pp. 232–237, Feb. 1999.

[16] G. I. Bell and S. Glasstone, *Nuclear reactor theory.* Van Nostrand Reinhold Co., New York, 1970.

[17] G. Arfken and H. Weber, *Essential Mathematical Methods for Physicists.* Harcourt/Academic Press, Burlington (MA), 2003.

[18] M. Balda, D. Niederlöhner, B. Heismann, B. Kreisler, and J. Durst, "Lookup Table-Based Simulation for Direct-Converting Counting X-Ray Detectors for CT," in *Nuclear Science Symposium Conference Record, IEEE*, 2009. Manuscript accepted, to be published January 2010.

[19] Personal communication with K. Mecke, Universität Erlangen-Nürnberg, 2008.

[20] B. Kreisler, G. Anton, J. Durst, and T. Michel, "Generalised adjoint simulation of induced signals in semiconductor X-ray pixel detectors," *Journal of Instrumentation*, vol. 3 P11002, 2008.

[21] COMSOL AB, Stockholm. www.comsol.de (October 2009).

[22] S. Patankar, *Numerical heat transfer and fluid flow.* Hemisphere Publishing Corporation, Washington, 1980.

[23] B. Kreisler, G. Anton, J. Durst, and T. Michel, "3D simulation of induced signals in the Medipix detector," in *Nuclear Science Symposium Conference Record, IEEE*, 2007.

[24] E. Gatti, A. Longoni, P. Rehak, and M. Sampietro, "Dynamics of Electrons in Drift Detectors," *Nucl. Instr. and Meth. A*, vol. 253, pp. 393–399, 1987.

[25] The MathWorks, Inc. www.mathworks.de (October 2009).

[26] J. Fink, H. Krüger, P. Lodomez, and N. Wermes, "Characterization of charge collection in CdTe and CZT using the transient current technique," *Nucl. Instr. and Meth. A*, vol. 560, pp. 435–443, 2006.

[27] Personal communication with D. Niederlöhner, Siemens AG, Healthcare Sector, 2009.

[28] International Commission on Radiological Protection, "103: Recommendations of the ICRP," Feb. 2008.

[29] R. L. Morin, T. C. Gerber, and C. H. McCollough, "Radiation Dose in Computed Tomography of the Heart," *Circulation*, vol. 107, pp. 917–922, 2003.

[30] T. Herrmann and M. Baumann, *Klinische Strahlenbiologie: kurz und bündig.* Gustav Fischer Verlag, Jena, 1997.

[31] R. Sauer, *Strahlentherapie und Onkologie.* Urban&Fischer Verlag, München, 4 ed., 2003.

[32] H. Nagasawa and J. Little, "Induction of Sister Chromatid Exchanges by Extremely Low Doses of α-Particles," *Cancer Research*, vol. 52, pp. 6394–6396, Nov. 1992.

[33] H. Krieger, *Strahlenphysik, Dosimetrie und Strahlenschutz*, vol. 1. Teubner, Stuttgart, 1998.

[34] P. Andreo and A. Brahme, "Mean energy in electron beams," *Med. Phys.*, vol. 8, pp. 682–687, 1981.

[35] P. Andreo, "Depth dose and stopping power data for monoenergetic electron beams," *Nucl. Instr. Meth. B*, vol. 51, pp. 107–121, 1990.

[36] H. Krieger, *Strahlenphysik, Dosimetrie und Strahlenschutz*, vol. 2. Teubner, Stuttgart, 1997.

[37] G. C. Bentel, *Radiation therapy planning.* McGraw-Hill Companies, Inc., 2 ed., 1996.

[38] S. Agostinelli, J. Allison, K. Amako, J. Apostolakis, H. Araujo, P. Arce, M. Asai, D. Axen, S. Banerjee, G. Barrand, F. Behner, L. Bellagamba, J. Boudreau, L. Broglia, A. Brunengo, H. Burkhardt, S. Chauvie, J. Chuma, R. Chytracek, G. Cooperman, G. Cosmo, P. Degtyarenko, A. Dell'Acqua, G. Depaola, D. Dietrich, R. Enami, A. Feliciello, C. Ferguson, H. Fesefeldt, G. Folger, F. Foppiano, A. Forti, S. Garelli, S. Giani, R. Giannitrapani, D. Gibin, J. J. G. Cadenas, I. González, G. G. Abril, G. Greeniaus, W. Greiner, V. Grichine, A. Grossheim, S. Guatelli, P. Gumplinger, R. Hamatsu, K. Hashimoto, H. Hasui, A. Heikkinen, A. Howard, V. Ivanchenko, A. Johnson, F. W. Jones, J. Kallenbach, N. Kanaya, M. Kawabata, Y. Kawabata, M. Kawaguti, S. Kelner, P. Kent, A. Kimura, T. Kodama, R. Kokoulin, M. Kossov, H. Kurashige, E. Lamanna, T. Lampén, V. Lara, V. Lefebure, F. Lei, M. Liendl, W. Lockman, F. Longo, S. Magni, M. Maire, E. Medernach, K. Minamimoto, P. M. de Freitas, Y. Morita, K. Murakami, M. Nagamatu, R. Nartallo, P. Nieminen, T. Nishimura, K. Ohtsubo, M. Okamura, S. O'Neale, Y. Oohata, K. Paech, J. Perl, A. Pfeiffer, M. G. Pia, F. Ranjard, A. Rybin, S. Sadilov, E. D. Salvo, G. Santin, T. Sasaki, N. Savvas, Y. Sawada, S. Scherer, S. Sei, V. Sirotenko, D. Smith, N. Starkov, H. Stoecker, J. Sulkimo, M. Takahata, S. Tanaka, E. Tcherniaev, E. S. Tehrani, M. Tropeano, P. Truscott, H. Uno, L. Urban, P. Urban, M. Verderi, A. Walkden, W. Wander, H. Weber, J. P. Wellisch, T. Wenaus, D. C. Williams, D. Wright, T. Yamada, H. Yoshida, and D. Zschiesche, "Geant4 - a simulation toolkit," *Nucl. Instr. and Meth. A*, vol. 506, pp. 250–303, 2003.

[39] J. Allison, K. Amako, J. Apostolakis, H. Araujo, P. Dubois, M. Asai, G. Barrand, R. Capra, S. Chauvie, R. Chytracek, G. Cirrone, G. Cooperman, G. Cosmo, G. Cuttone, G. Daquino, M. Donszelmann, M. Dressel, G. Folger, F. Foppiano, J. Generowicz, V. Grichine, S. Guatelli, P. Gumplinger, A. Heikkinen, I. Hrivnacova, A. Howard,

S. Incerti, V. Ivanchenko, T. Johnson, F. Jones, T. Koi, R. Kokoulin, M. Kossov, H. Kurashige, V. Lara, S. Larsson, F. Lei, O. Link, F. Longo, M. Maire, A. Mantero, B. Mascialino, I. McLaren, P. Lorenzo, K. Minamimoto, K. Murakami, P. Nieminen, L. Pandola, S. Parlati, L. Peralta, J. Perl, A. Pfeiffer, M. Pia, A. Ribon, P. Rodrigues, G. Russo, S. Sadilov, G. Santin, T. Sasaki, D. Smith, N. Starkov, S. Tanaka, E. Tcherniaev, B. Tome, A. Trindade, P. Truscott, L. Urban, M. Verderi, A. Walkden, J. Wellisch, D. Williams, D. Wright, and H. Yoshida, "Geant4 Developments and Applications," *IEEE Trans. Nucl. Sci.*, vol. 53, no. 1, pp. 270–278, 2006.

[40] S. Chauvie, S. Guatelli, V. Ivanchenko, F. Longo, A. Mantero, B. Mascialino, P. Nieminen, L. Pandola, S. Parlati, L. Peralta, M. G. Pia, M. Piergentili, P. Rodrigues, S. Saliceti, and A. Trindade, "Geant4 Low Energy Electromagnetic Physics," in *Nuclear Science Symposium Conference Record, IEEE*, 2004.

[41] www.cern.ch/geant4 (October 2009).

[42] P. Mayles, A. E. Nahum, and J.-C. Rosenwald, eds., *Handbook of radiotherapy physics: theory and practice.* CRC Press, Taylor & Francis Group, 2007.

[43] I. Münster, B. Kreisler, J. Durst, T. Michel, and G. Anton, "Simulation of a Medical Linac with Evaluation of Dose Profiles behind an Electron Applicator," in *Nuclear Science Symposium Conference Record, IEEE*, 2009. Manuscript accepted, to be published January 2010.

[44] A. Trindade, P. Rodrigues, L. Peralta, M. Lopes, C. Alves, and A. Chaves, "Fast electron beam simulation and dose calculation in radiotherapy," *Nucl. Instr. and Meth. A*, vol. 522, pp. 568–578, 2004.

[45] F. M. Khan, P. D. Higgins, B. J. Gerbi, F. C. Deibel, A. Sethi, and D. N. Mihailidis, "Calculation of depth dose and dose per monitor uni for irregular shaped electron fields," *Phys. Med. Biol.*, vol. 43, pp. 2741–2754, 1998.

[46] http://bugzilla-geant4.kek.jp/show_bug.cgi?id=1027 (October 2009).

[47] Physikalisch-Technische Werkstätten Dr. Pychlau GmbH, Freiburg, www.ptw.de (October 2009).

[48] E. B. Podgorsak, *Radiation physics for medical physicists.* Springer Verlag, Berlin Heidelberg New York, 2006.

Acknowledgements

Just before the end of this manuscript, I will take the chance to thank all the people who made my time at the institute worthwhile and contributed to this work in one way or another.
Let me begin with my supervisor Gisela Anton who always had her door open to me. It was a great opportunity to discuss about physics, but also different topics. Thank you for the time and the confidence.
But all the research presented in this work would have been very hard if not impossible without the support of my colleagues here at the ECAP (Erlangen Centre for Astroparticle Physics). I would like to point out some who are especially important for me: first of all, I have to express my gratitude to my two diploma students, Ina and Sebastian, not only for the valueable discussions on their topics, but also for the great atmosphere. Secondly, Jürgen has played a vital rule in the success of the work, as he always stayed close to the leading edge of my research and was a great help in many ways.
The medical physics group is steadily growing, so I cannot mention everybody indiviually, but there are a few with who I have shared many things while working here: Peter, Mike, Anja, Kati and Claudio. I must not miss the ones who left the institute in the last few years and still stay close: Markus & Karo, Frank & Susan. Thank you all for the time in and around the institute.
Thanks for the financial support by the International Max-Planck Research School for Optics and Imaging (IMPRS-OI). A special thanks also goes to our collaboration partners for their academic and personal interest in my work: Daniel, Silke, Björn, Gaby and Torsten.
I owe a lot to my parents and my entire family who always encouraged and supported me, so nothing would have been possible without them. And finally, I thank Annelen for a lot more than I can write down here.